Acta Geotechnica manuscript No.
(will be inserted by the editor)

Fault propagation and surface rupture in geologic materials with a meshfree continuum method

Enrique M. del Castillo · Alomir H. Fávero Neto · Ronaldo I. Borja

Received: date / Accepted: date

Abstract We utilize Smoothed Particle Hydrodynamics (SPH), a Lagrangian particle-based continuum method, to study the initiation and propagation of shear bands or faults in geologic materials over large deformations. We show that SPH is able to capture the formation of shear bands naturally without needing to introduce a heterogeneity or "seed". In an actively or passively loaded backfill behind a moving retaining wall, we show that shear bands crossing the surface are inclined at an orientation given by the Arthur angle, $\Theta_A = 45^\circ \pm (\psi + \phi)/4$, with respect to the principal stresses. Additionally, we conduct simulations to explore the fault propagation problem, where a blind fault in rigid basement rock propagates through an overlying weak layer to reach the surface. Our results demonstrate that the resulting shear band rotates as the blind fault progressively accumulates more slip, initially taking the orientation given by the Roscoe angle, $\Theta_R = 45^\circ \pm \psi/2$, then that of the Arthur angle, and lastly, that of the familiar Coulomb orientation, $\Theta_C = 45^\circ \pm \phi/2$, in both extensional and contractional setups. Finally, we also evaluate the validity of empirical solutions describing the shear band propagation path and consider the effect of different material parameters on the geometry of the resultant shear bands, as well as on displacement and deformation at the surface. Our results show that SPH deals well with external loadings such as those applied by a retaining wall, or those induced by tectonic movement like in the fault propagation problem.

Keywords Faulting · Folding · Meshfree continuum methods · Smoothed particle hydrodynamics · Strain localization

Enrique M. del Castillo · Ronaldo I. Borja
Department of Civil and Environmental Engineering, Stanford University, Stanford, CA 94305, USA
E-mail: borja@stanford.edu
Orcid: 0000-0002-7505-1705 (E.M. del Castillo)

Alomir H. Fávero Neto
Department of Civil and Environmental Engineering, Bucknell University, Lewisburg, PA 17837, USA

1 Introduction

As geologic materials such as rock or soil are subjected to non-homogeneous deformation, band-like zones of localized strain known as shear bands (also deformation bands or shear zones) form [11,15]. Shear band formation also frequently accompanies or precedes material rupture or faulting, and is generally a multiscale process [30,52,53,61,95,102]. In the vicinity of a fault, zones of significant strain localization accumulate surrounding the area where the material has ruptured, and thus a kinematic discontinuity is present across the shear band. Strain localization is an omnipresent and vital phenomenon in geomechanics and geotechnics as well as in the geophysical sciences, particularly in structural geology. Comprehending the patterns and shapes of strain localization is of utmost importance from scientific and engineering perspectives in problems where the failure of geomaterials is involved, such as in landslides, the slip surfaces in an earth or soil backfill behind a retaining wall, or the propagation of a fault and its associated deformation in a rock mass. For the geologist, knowledge of what boundary conditions produce particular strain localization patterns is also necessary to help reconstruct the tectonic history of a formation or, at a larger scale, a basin.

Strain localization phenomena have been mathematically explained and modeled using either bifurcation theory [12,15,78,89] or fracture mechanics [9,49,54,55,57]. Much effort has been made in accurately capturing strain localization patterns observed either experimentally in the laboratory or in the geological field records with computational methods such as the Finite Element Method (FEM). Nevertheless, some difficulties in modeling strain localization with FEM persist, namely, ambiguities as to where shear bands should originate [13,15] and the frequent need for the introduction of "seeds" or material heterogeneities into the model to induce strain localization [17,18,83,84]. To simulate the large deformations associated with certain classes of problems such as slippage of a fault, FEM and other mesh-based methods also require specialized frictional contact elements and element enhancements to circumvent the limitations of conventional finite element interpolation in capturing the development of localized deformation patterns [56,80]. Even without any kinematic discontinuity, conventional FEM simulations run the risk of mesh entanglement and distortion when modeling fault (or its proxy, shear band) propagation over long distances, requiring re-meshing that comes with a certain computational and accuracy penalty [47].

An alternative to FEM is Smoothed Particle Hydrodynamics (SPH), a meshfree, continuum-based, Lagrangian method, where particles represent pieces of a continuum body and thus possess continuum level field variables and properties such as mass, density, and velocity, among others. The values of these fields for each particle are determined by an interpolation from neighboring particles using a weighted sum and a kernel function. The meshfree nature of SPH allows it to handle large deformation problems, while having improved scalability over non-continuum meshfree methods such as the discrete element method (DEM) [63,88,99,100,103]. Furthermore, strain localization arises internally in an SPH code without the need for additional formulations or theory. In the case of faulting, while SPH may not resolve the precise rupture path through the discrete material points (or the exact length-scale of the strain localization), the meshfree nature still accommodates some level of deformation, and because the material points are Lagrangian, it can be argued, similar to what is done in DEM, that it is possible to

trace a fault in the midst of the surrounding region of strain localization. Furthermore, as demonstrated in this paper, kinematic discontinuities between otherwise continuous material layers can be achieved with SPH, suggesting that this method can in fact capture many macroscale properties of faulting. For the sake of lexical simplicity, zones of shear band development on the geological scale are henceforth considered synonymous to faulting, and thus the terms fault propagation or shear band propagation are used interchangeably.

SPH was initially developed by Lucy [60] and Gingold and Monaghan [39] for astrophysical applications, but has also had significant traction in computational fluid dynamics (CFD) applications [2] especially for free-surface flows [40], elastic dynamics [41], and more recently, in modeling the elastoplastic deformation of geomaterials [22,23,24,34,35,67,69]. In this paper we implement and use `GEOSPH`, a parallel SPH code built on the open source Python-based framework `PySPH` [72], extending current capabilities of the framework from primarily CFD applications, to be able to simulate the deformation of geomaterials, based on the formulation of Bui et al. [23] using elastoplasticity and the Drucker-Prager yield criterion. In our study, we first consider the formation of shear bands in an elastoplastic backfill behind a retaining wall, a classic problem in geotechnics, which we use to help validate our numerical implementation, but which also has great practical importance in geotechnics.

Next we consider the propagation of a blind fault in basement rock through an overlying weak layer and the folding produced by the propagating fault, illustrating the capacity of SPH to accurately model both problems. The SPH models are able to reproduce the expected geometry, kinematics, and strain localization patterns of other analogue and numerical experiments, while providing useful stress, strain, and strain rate data often absent from most non-continuum simulations. In the fault propagation problem, we also consider how properties of the propagating shear band (or fault) such as its orientation or inclination, are controlled by boundary conditions or by the material properties of the geomaterial host. Additionally, most previous applications of SPH for modeling geomaterials have focused on gravity-driven deformational processes such as granular collapses, flows, slope failures, or landslides [34,35,50,68,92,101]. Instead, in our retaining wall and fault propagation problems we simulate the external loading of material either through a retaining wall or a tectonic force, demonstrating SPH can handle these loadings and boundary conditions well.

The structure of our paper is organized as follows: Section 2 reviews the fault propagation problem and discusses previous studies in geotechnics and structural geology covering this topic. Section 3.1 presents the mechanical initial boundary-value problem and the necessary constitutive equations. Section 3.2 provides an overview of the SPH method and a description of our implementation. Moreover, Section 4 explores and validates the SPH code `GEOSPH` with the retaining wall problem, while Section 5 focuses on the process of fault propagation, which we simulate using `GEOSPH`. Lastly, Section 6 summarizes the results and findings of this paper as well as discusses potential future work.

2 Fault propagation and folding

The fault propagation problem refers to the propagation of a blind fault (a normal or reverse fault located in rigid basement rock) through weak layers that lie above it until it reaches the surface, in a process known as surface rupture. Fault propagation experiments generally belong to one of two kinematic regimes: extensional experiments under active loading conditions, where the blind fault is a normal fault and the hanging wall is pulled downwards along the blind fault as a result of the tectonic force, and contractional experiments under passive loading conditions where the blind fault is a reverse fault and the hanging wall is pushed upwards along the blind fault [70,71,85]. In the context of SPH, the propagating fault in the overlying weak material layer is visualized as a shear band (or a set of shear bands) emanating from the tip of the blind fault.

The fault propagation problem is closely associated to the topic of fault propagation folding, studied in structural geology, where the sediment or rock overlying the blind fault folds as a result of the fault propagation. More specifically, the sediment layers bend in the vertical direction in the vicinity of the penetrating fault forming a sequence of a monocline and syncline, with the exact kinematics depending on whether the basement fault and the overall slip are contractional or extensional. In the extensional case, the top surface undergoes a loss in height, so the monocline forms on the foot wall and the syncline on the hanging wall, while the reverse is true in the contractional case.

The monocline and syncline that form as a result of the propagated fault are known to be gas and oil traps, making their modeling of relevance for hydrocarbon exploration and exploitation [31,62]. Fault propagation folding in general is an almost ubiquitous feature of most sedimentary petroleum basins, adding to their relevance [36]. Furthermore, comprehending the mechanics of blind faults is of value due to the prevalence of earthquakes originating in them, such as the 1994 Northridge Earthquake [3,82], and the proximity of some blind faults to large urban areas such as the Wilmington blind thrust fault below Los Angeles [98]. The danger posed by blind faults is not limited to the elastic seismic waves, which are radiated from the fault plane. The displacement at the surface caused by the propagation of low-depth blind faults (a displacement often on the order of meters), can also be highly destructive as seen in the 1999 Kocaeli and Düzce earthquakes in Turkey, and the Chi-Chi earthquake in Taiwan [4,59]. The risk posed by fault propagation is not only pertinent to surface structures, but also to underground infrastructure such as tunnels, pipelines, and other utilities, which are vulnerable to large amounts of lateral displacement between the foot wall and hanging wall as the fault propagates [5,8].

Traditionally, in the geological sciences, fault propagation folding was studied using trishear [32] or parallel kink [86] kinematic models, based purely on geometric considerations, without any mechanistic underpinning. Meanwhile, in modeling studies, both analogue and numerical (primarily with DEM), the creation of realistic folding patterns, which resemble those observed in the field has been the main objective [36,37,43,79]. On the other hand, in the geotechnics community, centrifuge experiments together with DEM and FEM simulations have been the tools of choice, but research has focused on determining the propagation path and surface rupture location of the blind fault, as well as on expected surface dis-

placements, not on folding or the geological structures induced by the fault [6,45, 59].

While the fault propagation problem studied by both scholarly communities is similar in many aspects, in addition to the aforementioned differences in the objectives of the studies, the size of the problem and the amount of slip on the blind fault varies significantly in both geotechnics and geology versions of the problem. For example, normal faults resulting in fault propagation folding can occur on the basin scale, with the weak material layer being up to thousands of meters high, and surface displacements caused by fault propagation and surface rupture on the scale of hundreds if not thousands of meters [36,44]. Meanwhile, in the heavily studied 1999 Kocaeli earthquake, the blind faults were located at tens to hundreds of meters depth with the average surface displacement caused by surface rupture around 2.4 m [4]. In terms of the amounts of slippage of interest along the blind fault, on the basin scale, slip on the blind fault accumulates over geological time, resulting in vertical displacements of the blind fault of up to 20% or more of the total height ($U \geq 20\%H$) of the overlying material layer. In the geotechnics context, vertical displacements of up to $U = 10\%H$ are typically considered, as this is generally sufficient slip for a shallow blind fault to propagate to the surface in an earthquake.

In our study, we attempt to bridge the divide between the two disciplines. For example, we consider slip distances characteristic to both geotechnics and geological problems, and observe how empirical failure surface predictions (those of Cole and Lade [27]) devised for geotechnics-scale experiments perform for geological-scale slip amounts. For geotechnics applications, to help mitigate the risk of fault propagation, it is important to predict the path of fault propagation, the location of surface rupture s, the expected amount of surface displacement Δy, and the amount of blind fault slip d_{cr} required for the fault to rupture at the surface, among other quantities. We determine these properties and quantities and explore how they are affected by varying boundary conditions such as the blind fault dip angle θ. In our study, we also determine the material properties of the weak layer overlying the blind fault that could cause the greatest damage to overlying structures and the built environment.

In addition to our novel framing of the fault propagation problem, linking the geological with the geotechnics scales, our study also has the great advantage that our simulations using SPH can easily handle large slippage amounts on the blind fault characteristic of geological scale problems, which previously had been primarily studied using DEM or analogue sandbox-style experiments due to the large deformations involved. As mentioned before, another advantage of using SPH is that it can handle these large deformation levels while providing continuum scale stress, strain, and strain rate information, as is done routinely in geotechnics-scale fault propagation simulations using FEM.

3 Governing equations and SPH implementation

3.1 Governing and constitutive equations

Focusing only on the mechanical response, the SPH implementation solves the conservation of linear momentum with prescribed initial and boundary conditions.

For a domain Ω with boundary Γ such that $\bar{\Omega} = \Omega \cup \Gamma$, $\Gamma = \overline{\Gamma_v \cup \Gamma_h}$, and $\varnothing = \overline{\Gamma_v \cap \Gamma_h}$, the strong form of the initial boundary-value problem (IBVP) is written as follows: Given $\boldsymbol{b}\colon \Omega \to \mathbb{R}^3$, $\bar{\boldsymbol{v}}\colon \Gamma_v \to \mathbb{R}^3$, and $\boldsymbol{h}\colon \Gamma_h \to \mathbb{R}^3$, find $\boldsymbol{u}\colon \bar{\Omega} \to \mathbb{R}^3$, such that:

$$\nabla \cdot \boldsymbol{\sigma} + \boldsymbol{b} = \rho \dot{\boldsymbol{v}} \quad \forall \boldsymbol{x} \text{ in } \Omega \times t\,, \tag{1}$$

$$\boldsymbol{v} = \bar{\boldsymbol{v}} \quad \text{on } \Gamma_v \times t\,, \tag{2}$$

$$\boldsymbol{\sigma} \cdot \boldsymbol{n} = \boldsymbol{h} \quad \text{on } \Gamma_h \times t\,, \tag{3}$$

subject to initial conditions $\boldsymbol{u} = \boldsymbol{u}_0$, $\boldsymbol{v} = \boldsymbol{v}_0$, and $\dot{\boldsymbol{v}} = \dot{\boldsymbol{v}}_0$ at time $t = 0$. In the previous IBVP, $\dot{\boldsymbol{v}}$ represents the material time derivative of the velocity field, $\boldsymbol{b}$ is the body force vector, $\boldsymbol{u}$ is the displacement field vector, $\boldsymbol{n}$ is the unit normal vector to boundary Γ_h, and $\boldsymbol{\sigma}$ is the Cauchy stress tensor; $\bar{\boldsymbol{v}}$ and $\boldsymbol{h}$ are prescribed velocity and traction vectors, respectively.

Let $\boldsymbol{v} = \boldsymbol{v}(\boldsymbol{x}, t)$ and let the velocity gradient be defined as $\boldsymbol{l} = \partial \boldsymbol{v}/\partial \boldsymbol{x}$. The rate of deformation tensor $\boldsymbol{d}$ and spin tensor $\boldsymbol{\omega}$ are the symmetric and skew-symmetric parts of $\boldsymbol{l}$, i.e.,

$$\boldsymbol{d} = \frac{1}{2}\left(\boldsymbol{l} + \boldsymbol{l}^T\right), \qquad \boldsymbol{\omega} = \frac{1}{2}\left(\boldsymbol{l} - \boldsymbol{l}^T\right). \tag{4}$$

The rate of deformation tensor is assumed to be decomposed additively into elastic and plastic parts as follows,

$$\boldsymbol{d} = \boldsymbol{d}^e + \boldsymbol{d}^p\,. \tag{5}$$

A hypoelastoplastic model is defined by a direct relation between an objective stress rate tensor and the rate of deformation tensor. Here, we consider the Jaumann rate as the objective stress rate [73],

$$\overset{\triangledown}{\boldsymbol{\sigma}} = \dot{\boldsymbol{\sigma}} - \boldsymbol{\omega} \cdot \boldsymbol{\sigma} + \boldsymbol{\sigma} \cdot \boldsymbol{\omega}\,. \tag{6}$$

The rate-constitutive equation then takes the form

$$\overset{\triangledown}{\boldsymbol{\sigma}} = \bar{\boldsymbol{c}} : \boldsymbol{d}\,, \tag{7}$$

where $\bar{\boldsymbol{c}}$ is the rank-four tensor of tangential moduli. Substituting Equation (7) into (6) and solving for the Cauchy stress rate yields

$$\dot{\boldsymbol{\sigma}} = \bar{\boldsymbol{c}} : \boldsymbol{d} + \boldsymbol{\omega} \cdot \boldsymbol{\sigma} - \boldsymbol{\sigma} \cdot \boldsymbol{\omega}\,. \tag{8}$$

The tensor $\bar{\boldsymbol{c}}$ is a material response tensor and typically depends on the stress and deformation states along with some material parameters. For an elastic-perfectly plastic material with yield function $\mathcal{F}$ and plastic potential function $\mathcal{Q}$, the expression for the material response tensor is $\bar{\boldsymbol{c}} = \boldsymbol{c}^{\mathrm{e}}$ in the elastic regime and $\bar{\boldsymbol{c}} = \boldsymbol{c}^{\mathrm{ep}}$ in the plastic regime, where

$$\boldsymbol{c}^{\mathrm{ep}} = \boldsymbol{c}^{\mathrm{e}} - \frac{1}{\chi}\boldsymbol{c}^{\mathrm{e}} : \frac{\partial \mathcal{Q}}{\partial \boldsymbol{\sigma}} \otimes \frac{\partial \mathcal{F}}{\partial \boldsymbol{\sigma}} : \boldsymbol{c}^{\mathrm{e}} \tag{9}$$

and

$$\chi = \frac{\partial \mathcal{F}}{\partial \boldsymbol{\sigma}} : \boldsymbol{c}^{\mathrm{e}} : \frac{\partial \mathcal{Q}}{\partial \boldsymbol{\sigma}}\,. \tag{10}$$

For an isotropic material, the elastic material response tensor may be written in terms of the elastic bulk and shear moduli K and μ, respectively, and takes the form

$$\boldsymbol{c}^{\mathrm{e}} = K\mathbf{1}\otimes\mathbf{1} + 2\mu\Big(\boldsymbol{I} - \frac{1}{3}\mathbf{1}\otimes\mathbf{1}\Big)\,, \tag{11}$$

where $\boldsymbol{I}$ is the rank-four symmetric identity tensor with components $I_{ijkl} = (\delta_{ik}\delta_{jl} + \delta_{il}\delta_{jk})/2$ and $\mathbf{1}$ is the second-order identity tensor consisting of the Kronecker delta.

In the plastic regime, yielding is assumed to be governed by the Drucker-Prager yield criterion with yield function

$$\mathcal{F}(I_1, J_2) = \sqrt{2J_2} + \alpha_\phi I_1 - k_c \leq 0\,, \tag{12}$$

where $J_2 = \|\boldsymbol{s}\|^2/2$ is the second invariant of the deviatoric stress tensor, $\boldsymbol{s}$, and $I_1 = \mathrm{tr}[\boldsymbol{\sigma}]$ is the first invariant of the Cauchy stress tensor. The parameters α_ϕ and k_c are related to the angle of internal friction ϕ and cohesion c of the material, and are given by

$$\alpha_\phi = \frac{\sqrt{2}\tan\phi}{\sqrt{9+12\tan^2\phi}} \quad \text{and} \quad k_c = \frac{3\sqrt{2}c}{\sqrt{9+12\tan^2\phi}}\,. \tag{13}$$

Geologic materials typically follow a non-associative flow rule, which means that $\mathcal{Q} \neq \mathcal{F}$. In this work, we take the plastic potential function as

$$\mathcal{Q} = \sqrt{2J_2} + \alpha_\psi I_1 \tag{14}$$

where α_ψ is related to the dilation angle ψ via the equation

$$\alpha_\psi = \frac{\sqrt{2}\tan\psi}{\sqrt{9+12\tan^2\psi}}\,. \tag{15}$$

The Drucker-Prager parameters given above are for plane strain analyses. For more details about the Drucker-Prager model and its parameters for 3D conditions, the reader is referred to [14].

Given the algorithmic format for dynamic analysis employed by the SPH technique, an explicit stress-point integration is herein employed to advance the solution over finite increments. From Equation (8), the Cauchy stress rate is integrated over time as follows,

$$\boldsymbol{\sigma}_{n+1} = \hat{\boldsymbol{\sigma}}_n + \Delta t\bar{\boldsymbol{c}}_n : \boldsymbol{d}_n\,, \tag{16}$$

where

$$\hat{\boldsymbol{\sigma}}_n = \boldsymbol{\sigma}_n + \boldsymbol{R}\cdot\boldsymbol{\sigma}_n - \boldsymbol{\sigma}_n\cdot\boldsymbol{R}\,, \qquad \boldsymbol{R} = \Delta t\boldsymbol{\omega}_n\,. \tag{17}$$

Note that an explicit computation of the rotation tensor $\boldsymbol{R}$ is acceptable only if the material undergoes small rotation within the time interval of interest. For large rotations within a given time interval, an objective algorithm for integrating the rate constitutive equations must be employed, such as the one proposed by Hughes and Winget (1980) [48]. Furthermore, an explicit stress-point integration algorithm is susceptible to drift that could lead to the stress point going outside of the yield surface. Standard corrections may be employed in the present algorithm to correct for stress drift [23].

3.2 SPH implementation

In the SPH method, the continuous problem domain is discretized into an assembly of particles, which possess continuum level properties such as mass, density, velocity, etc. The value of each material property, denoted $f(\boldsymbol{x})$, is found for a particular particle using the following convolution integral over the domain Ω.

$$\langle f(\boldsymbol{x})\rangle = \int_{\Omega} f(\boldsymbol{x'})W(\boldsymbol{x}-\boldsymbol{x'},h)\mathrm{d}\boldsymbol{x'}\,. \tag{18}$$

Here, $W : \mathbb{R}^3 \times \mathbb{R}^+ \to \mathbb{R}^+$ is the kernel (or smoothing function) which serves as a weighting function, and h is the smoothing length, which controls the size of the integration domain Ω. The kernel function W must satisfy (among others) the three following conditions:

$$\int_{\Omega} W(\boldsymbol{x}-\boldsymbol{x'},h)\mathrm{d}\boldsymbol{x'} = 1\,, \tag{19}$$

$$\lim_{h\to 0} W(\boldsymbol{x}-\boldsymbol{x'},h) = \delta(\boldsymbol{x}-\boldsymbol{x'})\,, \tag{20}$$

$$W(\boldsymbol{x}-\boldsymbol{x'},h) = 0 \text{ when } |\boldsymbol{x}-\boldsymbol{x'}| > k_w h\,, \tag{21}$$

where δ is the Dirac-delta distribution and k_w is a constant that helps define the support domain of radius $k_w h$ for the particle. The smoothing length h is taken to be $h = k_h \Delta$, where Δ is the initial inter-particle distance, and k_h is a constant known as the smoothing length factor. Equation (19) is known as the normalization condition, Equation (20) as the delta function property, and Equation (21) as the compact support condition. In this study we use the Wendland Quintic C2 kernel, which is written as

$$W(q,h) = \begin{cases} \alpha_d(1-q/2)^4(2q+1), & \text{for } 0 \le q \le 2, \\ 0, & \text{for } q > 2, \end{cases} \tag{22}$$

where $q = |\boldsymbol{x}-\boldsymbol{x}'|/h$ is the normalized distance between particles i and j, and the constant α_d takes the values of $\alpha_d = 7/4\pi h^2$ in two dimensions and $\alpha_d = 21/16\pi h^3$ in three dimensions [96].

The derivative of a material property $\partial f(\boldsymbol{x})/\partial \boldsymbol{x}$ is found by replacing $f(\boldsymbol{x'})$ with $\partial f(\boldsymbol{x'})/\partial \boldsymbol{x'}$ in Equation (18) and then using integration by parts and the divergence theorem, which gives the expression

$$\left\langle \frac{\partial f(\boldsymbol{x})}{\partial \boldsymbol{x}} \right\rangle = \int_S f(\boldsymbol{x'})W(\boldsymbol{x}-\boldsymbol{x'},h)\cdot \boldsymbol{n}\mathrm{d}S - \int_{\Omega} f(\boldsymbol{x'})\frac{\partial W(\boldsymbol{x}-\boldsymbol{x'},h)}{\partial \boldsymbol{x'}}\mathrm{d}\boldsymbol{x'}\,, \tag{23}$$

where S represents the surface of the domain of integration Ω and $\boldsymbol{n}$ is the unit normal to S. Note that the surface integral on the right hand side of the expression equals zero for an internal particle in the domain since W has compact support. Furthermore, writing the derivative with respect to $\boldsymbol{x}$ instead of $\boldsymbol{x'}$ flips the sign of

the last integral. Hence, the integral approximation of the derivative of a material property is given by:

$$\left\langle \frac{\partial f(\boldsymbol{x})}{\partial \boldsymbol{x}} \right\rangle = \int_{\Omega} f(\boldsymbol{x'}) \frac{\partial W(\boldsymbol{x} - \boldsymbol{x'}, h)}{\partial \boldsymbol{x}} \mathrm{d}\boldsymbol{x'} \,. \tag{24}$$

The continuous integral for the material property $f(\boldsymbol{x})$ for particle i at position $\boldsymbol{x}$ can be approximated by the summation

$$\langle f(\boldsymbol{x}) \rangle_i \approx \sum_{j=1}^{N} \frac{m_j}{\rho_j} f(\boldsymbol{x}_j) W(\boldsymbol{x}_i - \boldsymbol{x}_j, h) \,, \tag{25}$$

over all particles j in the support domain of i. Likewise, $\partial f(\boldsymbol{x})/\partial \boldsymbol{x}$ for particle i can be approximated by

$$\left\langle \frac{\partial f(\boldsymbol{x})}{\partial \boldsymbol{x}} \right\rangle_i \approx \sum_{j=1}^{N} \frac{m_j}{\rho_j} f(\boldsymbol{x}_j) \left[\frac{\partial W(\boldsymbol{x} - \boldsymbol{x}_j, h)}{\partial \boldsymbol{x}} \right]_i \,. \tag{26}$$

These relations are expressed using simplified notation as

$$f(\boldsymbol{x}_i) = \sum_{j=1}^{N} \frac{m_j}{\rho_j} f(\boldsymbol{x}_j) W_{ij} \,, \tag{27}$$

$$\left. \frac{\partial f(\boldsymbol{x})}{\partial \boldsymbol{x}} \right|_i = \sum_{j=1}^{N} \frac{m_j}{\rho_j} f(\boldsymbol{x}_j) \cdot \frac{\partial W_{ij}}{\partial \boldsymbol{x}_i} \,, \tag{28}$$

where $W_{ij} = W(\boldsymbol{x}_i - \boldsymbol{x}_j, h)$ and

$$\frac{\partial W_{ij}}{\partial \boldsymbol{x}_i} = \left(\frac{\boldsymbol{x}_i - \boldsymbol{x}_j}{r} \right) \frac{\partial W_{ij}}{\partial r} \tag{29}$$

with $r = |\boldsymbol{x}_i - \boldsymbol{x}_j|$ the distance between particles i and j.

There are many ways in which Equation (28) can be used to approximate the gradient of a field function. For more details on this, the reader is referred elsewhere [91]. In our work, the velocity gradient for each particle i, $\boldsymbol{l}_i = \partial \boldsymbol{v}(\boldsymbol{x})/\partial \boldsymbol{x}\big|_i$ is approximated as

$$\boldsymbol{l}_i = \sum_{j=1}^{N} \frac{m_j}{\rho_j} (\boldsymbol{v}_j - \boldsymbol{v}_i) \otimes \frac{\partial W_{ij}}{\partial \boldsymbol{x}_i} \,. \tag{30}$$

Conservation of mass needs to be explicitly solved in the standard SPH formulation. Since the mass of any particle is kept constant throughout the simulations, the density of particle i is updated over time. Hence, from the continuity equation, we approximate the time rate of change of density as

$$\dot{\rho}_i = \sum_{j=1}^{N} m_j (\boldsymbol{v}_i - \boldsymbol{v}_j) \cdot \frac{\partial W_{ij}}{\partial \boldsymbol{x}_i} \,. \tag{31}$$

Furthermore, the conservation of linear momentum, Equation (1), is expressed as

$$\dot{\boldsymbol{v}}_i = \sum_{j=1}^{N} m_j \left(\frac{\boldsymbol{\sigma}_i + \boldsymbol{\sigma}_j}{\rho_i \rho_j} \right) \cdot \frac{\partial W_{ij}}{\partial \boldsymbol{x}_i} + \boldsymbol{g} \,, \tag{32}$$

where $\boldsymbol{g}$ is the gravitational acceleration vector. Finally, we discretize $\boldsymbol{d}_i$ and $\boldsymbol{\omega}_i$ as well.

$$\boldsymbol{d}_i = \frac{1}{2}\left(\boldsymbol{l}_i + \boldsymbol{l}_i^T\right) = \frac{1}{2}\Big[\sum_{j=1}^{N} \frac{m_j}{\rho_j}\left(\boldsymbol{v}_j - \boldsymbol{v}_i\right) \otimes \frac{\partial W_{ij}}{\partial \boldsymbol{x}_i} + \Big(\sum_{j=1}^{N} \frac{m_j}{\rho_j}(\boldsymbol{v}_j - \boldsymbol{v}_i) \otimes \frac{\partial W_{ij}}{\partial \boldsymbol{x}_i}\Big)^T\Big], \quad (33)$$

$$\boldsymbol{\omega}_i = \frac{1}{2}\left(\boldsymbol{l}_i - \boldsymbol{l}_i^T\right) = \frac{1}{2}\Big[\sum_{j=1}^{N} \frac{m_j}{\rho_j}\Big(\boldsymbol{v}_j - \boldsymbol{v}_i\Big) \otimes \frac{\partial W_{ij}}{\partial \boldsymbol{x}_i} - \Big(\sum_{j=1}^{N} \frac{m_j}{\rho_j}(\boldsymbol{v}_j - \boldsymbol{v}_i) \otimes \frac{\partial W_{ij}}{\partial \boldsymbol{x}_i}\Big)^T\Big]. \quad (34)$$

Despite the many advantages of SPH over mesh-based methods such as FEM, like any numerical method, SPH also exhibits some undesirable numerical features, including non-physical oscillations in the stress field (zero-energy modes) and a tendency for elastic shock waves to form within the simulated material [23,58]. To surmount the formation of shock waves and ameliorate stress oscillation, a dissipative term known as the artificial viscosity [58], Π_{ij} is introduced into the conservation of momentum to stabilize the equation and reduce shock waves,

$$\dot{\boldsymbol{v}}_i = \sum_{j=1}^{N} m_j\Big(\frac{\boldsymbol{\sigma}_i + \boldsymbol{\sigma}_j}{\rho_i \rho_j} + \Pi_{ij}\mathbf{1}\Big) \cdot \frac{\partial W_{ij}}{\partial \boldsymbol{x}_i} + \boldsymbol{g}\,, \quad (35)$$

where

$$\Pi_{ij} = \begin{cases} \dfrac{\alpha_\pi \bar{c}_{ij}\phi_{ij} - \beta_\pi \phi_{ij}^2}{\bar{\rho}_{ij}} & \text{for } \boldsymbol{v}_{ij}\cdot\boldsymbol{x}_{ij} < 0\,, \\ 0 & \text{for } \boldsymbol{v}_{ij}\cdot\boldsymbol{x}_{ij} \geq 0\,, \end{cases} \quad (36)$$

with

$$\phi_{ij} = \frac{h_{ij}\boldsymbol{v}_{ij}\cdot\boldsymbol{x}_{ij}}{|\boldsymbol{x}_{ij}|^2 + \eta^2}\,, \quad (37)$$

where for particles i and j, $\bar{c}_{ij} = (c_i + c_j)/2$, $\bar{\rho}_{ij} = (\rho_i + \rho_j)/2$, $h_{ij} = (h_i + h_j)/2$, $\boldsymbol{x}_{ij} = \boldsymbol{x}_i - \boldsymbol{x}_j$, $\boldsymbol{v}_{ij} = \boldsymbol{v}_i - \boldsymbol{v}_j$, and $\eta \sim 0.01h$. The coefficients α_π and β_π are two constants which usually assume values between 0 and 1, c is the numerical speed of sound for the particles, ρ is the particle density, and h is the smoothing length. The numerical speed of sound for particle i is calculated as

$$c_i = \max\Big(\sqrt{\frac{E}{\rho}}, \sqrt{\frac{K}{\rho}}\Big)_i\,. \quad (38)$$

Another undesirable feature characteristic to SPH is the so-called tensile instability, where particles tend to attract one another when the material is under tension, leading to the formation of clumps or chains. To resolve this issue, Gray and Monaghan [41] introduced a correction called artificial stress, where a small hydrostatic compressive stress S_{ij} is added to the balance of linear momentum. This compressive stress generates a short-ranged repulsive force used when the material is subject to tension to prevent clumping. Rather than using the original

artificial stress implementation, a simplified version proposed by Peng et al. [67], is used where

$$S_{ij} = f_{ij}^{n} \left(R_i + R_j \right), \tag{39}$$

and where the components of R_i are given by:

$$R_i = \begin{cases} \epsilon \dfrac{p_i}{\rho_i^2} & \text{for } p_i > 0\,, \\ 0 & \text{for } p_i \leq 0\,. \end{cases} \tag{40}$$

In the previous equations, ϵ is a coefficient in the range 0 to 1, p_i is the hydrostatic stress for particle i, n ranges from 2 to 6, and f_{ij} is given by:

$$f_{ij} = \frac{W_{ij}}{W(\Delta x)}\,, \tag{41}$$

where Δx is the initial interparticle distance. The term S_{ij} is another stabilization term and is introduced in the conservation of linear momentum in a similar fashion to the artificial viscosity. Hence, the final SPH approximation for the conservation of linear momentum is as follows

$$\dot{\boldsymbol{v}}_i = \sum_{j=1}^{N} m_j \left[\frac{\boldsymbol{\sigma}_i + \boldsymbol{\sigma}_j}{\rho_i \rho_j} + \left(\Pi_{ij} - S_{ij} \right) \mathbf{1} \right] \cdot \frac{\partial W_{ij}}{\partial \boldsymbol{x}_i} + \boldsymbol{g}\,. \tag{42}$$

Given that the SPH method is a continuum meshless and Lagrangian method, the IBVP domain is discretized with a set of arbitrarily distributed particles that serve not only as mathematical points to solve the balance equations, but also act as physical points carrying all of the field variables of the problem. The solution is evolved over time using any explicit time integration scheme such as the forward Euler, Predictor-Corrector, or Leap-Frog. In our work, we chose a variation of the forward Euler scheme, which has optimum conservation properties [91]. In this scheme, given a field variable and its rate of change at the beginning of a time step n, corresponding to a simulation time t_n, the updated value of that field variable at the beginning of the next time step, $n+1$ at t_{n+1} is given by:

$$f(\boldsymbol{x})_{n+1} = f(\boldsymbol{x})_n + \dot{f}(\boldsymbol{x})_n \Delta t\,, \tag{43}$$

where $\dot{f}$ is the material time derivative of the field variable, and $\Delta t = t_{n+1} - t_n$ is the time step.

The time step is determined using the CFL stability conditions. Hence, the time step is then limited to

$$\Delta t \leq a \frac{h}{c}\,, \tag{44}$$

where a is the CFL parameter and was chosen to be 0.1 for the simulations in this paper.

For geotechnical and geosciences applications, the initial state of stress and deformation of the geomaterials is very important. In all of our simulations we applied gravity and a damping term that enabled particles to reach equilibrium positions and a geostatic state of stress. After the equilibrium was obtained (minimum kinetic energy), the plastic deformations were set to zero, and the geostatic state of stress and elastic deformation were used as initial conditions for the remainder

of the simulations. The damping term used in the initialization simulations was applied directly to the right-hand side of the balance of linear momentum and had the form:

$$\boldsymbol{D}_i = -\zeta \boldsymbol{v}_i \,, \tag{45}$$

where ζ is a coefficient determined following the work of Colagrossi et al. [26] as

$$\zeta = \xi \frac{c}{h} \,, \tag{46}$$

with ξ between 0 and 1, and chosen to be 0.1 for our initialization simulations. Note that the damping term was turned off after the initialization simulations were over and the initial state of stress and strain defined.

Another important aspect of SPH is the treatment of Dirichlet boundary conditions. In our work, we used the dynamic boundary condition formulation proposed by Adami et al. [1]. In this approach, the solid boundaries are discretized using layers of particles that are fixed or move with a prescribed velocity, while their other properties remain constant, with exception to stress. Following Adami's work, the stress of the boundary particles is updated with time by extrapolation of the state of stress of the domain particles. Differently from the original work of Adami and his co-authors, we do not update the density of the boundary particles.

In all of the simulations presented in this paper, we applied the artificial viscosity term with parameters $\alpha_\pi = 0.2$ and $\beta_\pi = 0.4$. Moreover, we assumed perfect plasticity in the constitutive model. For simulations with cohesion, where tensile stresses may occur, we also applied the artificial stress term with $\epsilon = 0.2$. Finally, due to the so-called "particle inconsistency" of the SPH method, the kernel gradient was corrected to guarantee first-order consistency of the SPH interpolation operators. For further details on the kernel gradient correction, the reader is referred to the paper of Bonet and Lok [10]. For a complete overview of the SPH method, details of implementation, and a listing of the code we developed, please refer to the work of Fávero Neto [33]. In the next section we present some of the simulations used to validate `GEOSPH`.

4 Shear band formation behind a retaining wall

In the classic geotechnics problem involving a retaining wall holding back a granular backfill, yielding of the backfill can occur under two extreme conditions: active condition when the soil is stretched horizontally, and passive condition when the soil is compressed horizontally. In the Coulomb [28] and Rankine [74] limit equilibrium theories of lateral earth pressure on retaining walls, the failure surface is assumed to be straight and planar, and soil mass in the backfill is a rigid wedge with the failure surface inclined with respect to the principal stress (acting horizontally for a smooth wall) at $\Theta = 45^\circ \pm \phi/2$, a value also commonly known as the Coulomb angle Θ_C, with $\Theta = 45^\circ + \phi/2$ under active loading condition and $\Theta = 45^\circ - \phi/2$ under passive condition. Similar analytical expressions for the orientation of the failure planes were also given in later studies by Arthur [7] and Roscoe [77], with the so-called Arthur angle $\Theta_A = 45^\circ \pm (\phi + \psi)/4$ and the so-called Roscoe angle $\Theta_R = 45^\circ \pm \psi/2$ with respect to the horizontal.

While today's experimental observation and more sophisticated analytical and numerical studies have indicated that the failure surface in passive and active

loading cases is not a straight surface, but rather exhibits some amount of curvature, the Coulomb, Arthur, and Roscoe predictions are still valuable references. For non-smooth retaining walls, Caquot and Kerisel [25] provided a theoretical limit-equilibrium solution for the passive and active states where the failure surface is assumed to be a logarithmic spiral. At the top surface of the backfill, the failure surface is oriented by the Coulomb angle with respect to the horizontal (see Figure 1). Additionally, the location of the passive earth pressure force P_p along the face of the retaining wall is pre-selected to be at a height of $H/3$. According to their solution, the normal component of the active force is $P_n = K_a \gamma \cos(\delta) H^2/2$ and the vertical component is $P_v = K_a \gamma \sin(\delta) H^2/2$, where δ is the soil-to-wall friction angle, γ is the unit weight of the soil, and K_a is the coefficient of active earth pressure. In the passive state the active coefficient K_a is replaced with the passive coefficient K_p in the expressions for P_n and P_v. The values of these coefficient are tabulated in the NAVFAC Design Manual DM7.02 (1986) for different values of the ratio δ/ϕ [29].

In this work, a series of validation tests are conducted to verify the performance of our `GEOSPH` implementation against previous studies of the retaining wall problem. For the backfill, a 5 m high and 10 m long backfill is used for the active case, with a mobile retaining wall located on the left side of the backfill and a static wall located on the right side (see Figure 1). All the wall boundaries are modeled using boundary particles. In the passive case the same setup is used with the exception that the backfill length is doubled to 20 m to allow the failure surface to emerge freely on the top surface without interference from the static wall. The backfill is modeled as an elastic-perfectly plastic material with the material parameters given in Table 1 and represented by 6,096 particles. The material parameters selected for the backfill are chosen to be the same as those used by Borja and Lai [16] to facilitate comparison, and are not meant to be representative of an actual soil backfill. Instead, they are picked so that at K_0 condition all points within the backfill yield from imposing the gravity load alone.

For the purposes of a sensitivity analysis, simulations using finer and coarser discretizations were performed by varying the particle spacing to $\Delta = 0.05$ and 0.15 m with 24,384 and 2,710 particles respectively, but yield indistinguishable results with respect to the original $\Delta = 0.1$ m discretization in terms of the failure mechanism, and shear band patterns. Sensitivity analyses carried out for the other simulations shown in the paper achieved similar results, although some minor variation in the shear band thickness was observed; i.e., the bands widened slightly with coarser discretizations. However, due to the nonlocal nature of SPH stemming from the smoothing length h, which is a numerical characteristic length scale, the sensitivity of the shear band width to the spatial discretization can be eliminated by selecting a value of k_h that ensures the smoothing length is maintained fixed as the discretization (or the inter-particle distance) changes [90]. Simulations of varying discretization resolution while keeping h constant revealed that the shear band thickness remained unchanged. Thus, if the shear band thickness is known apriori, we can adjust the SPH resolution (and hence, the smoothing length) to accommodate for this thickness.

In the simulations, the active loading case is enforced by pulling the retaining wall from the backfill ($-\Delta x$), while in the passive loading case the retaining wall is pushed into the backfill ($+\Delta x$). SPH is known to exhibit rate-dependent behavior when external loading is applied to the boundaries if the sustained equivalent strain

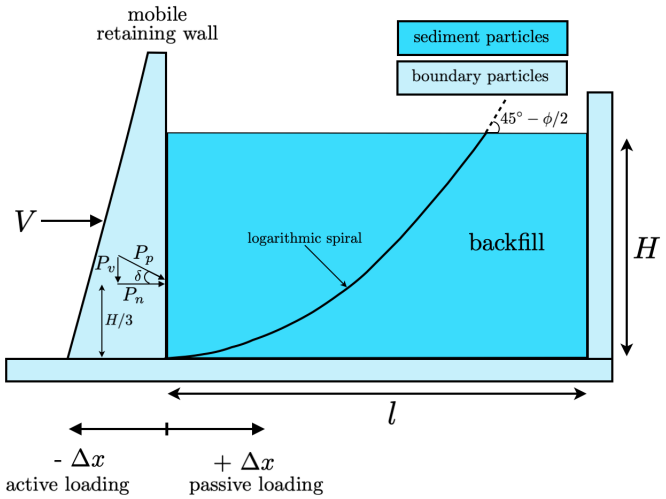

Fig. 1: Boundary value problem setup for the retaining wall problem, here showing V pointing in the direction of passive loading. The theoretical logarithmic spiral failure surface of Caquot and Kerisel [25] and the components of the passive pressure P_p are also displayed.

rate is greater than 0.1 s^{-1} [94]. For strain rates below this threshold, quasi-static solutions can be achieved that reduce the strain rate dependency. Thus, the wall is moved with a velocity of $V = 0.01$ m/s to yield equivalent strain rates below the 0.1 s^{-1} threshold.

Table 1: Simulation parameters for the retaining wall experiments.

Parameter	**Value**
Density, ρ [kg/m^3]	2000
Particle mass, m [kg]	20
Time step, Δt [s]	0.0001
Initial inter-particle distance, Δ [m]	0.1
Smoothing length factor, k_h	1.5
Poisson Ratio, ν	0.3
Young's Modulus, E [kPa]	26,000
Artificial viscosity parameters, α_π and β_π	0.2 and 0.4
Artificial stress parameter, ϵ	0.2
Cohesion, c [kPa]	0
Internal friction angle, ϕ [°]	23.1
Dilation angle, ψ [°]	10.6
Pushing or pulling velocity, V [m/s]	0.01
Height, H [m]	5
Length, l [m]	10 or 20

As the retaining wall is slowly pulled away from the backfill to simulate active failure, the bottom left corner of the backfill undergoes plastic strain localization after 0.01 m of wall displacement, as seen in the plots of the accumulated plas-

tic strain ε^p_{acc} (calculated from time-integrating $\|\boldsymbol{d}^p\|$) and volumetric strain ε_{vol} (calculated from time-integrating $\mathrm{tr}(\boldsymbol{d})$) in columns (a) and (b) of Figure 2, respectively. A shear band then propagates towards the top surface along a mostly straight inclined trajectory with some slight curvature, resembling a log spiral and is fully traced after $\Delta x = 0.08$ m. After 0.16 m of wall displacement, vertical subsidence of the top surface is visible in the area between the shear band and the retaining wall. This subsidence and the shear band geometry are similar to the results of a combination of centrifuge, FEM, and DEM results reported by Widuliński et al. [97]. Comparing with the FEM analysis of Borja and Lai [16] for a smooth wall, localization first occurred after 0.016 m wall displacement, and the shear band was fully traced around 0.06 m wall displacement.

Because the retaining wall in our simulations was rough, with a frictional coefficient of $\delta = 0.79\phi$, we also evaluate the normal (P_n) and vertical (P_v) components of the active force over displacement against the theoretical limit equilibrium solutions provided by NAVFAC Design Manual DM7.02 [29] in Figure 3. As expected from the force-displacement curves, in panel (a) a rapid drop in normal force follows the initiation of wall movement, and the change in the normal active force on the retaining wall with respect to wall displacement decreases around the time when the shear band is fully traced. However, a complete plateau in the force-displacement curve, which would be indicative of the residual state expected for a wedge solution failure plane, or of the NAVFAC limit equilibrium solution, is not reached, due to the evident curvature of the shear band. A similar situation occurs with the vertical force P_v in Figure 3, panel (b), although the decrease in force is more resemblant of a plateau once the shear band is fully traced. This is due to the evolving geometry of the wedge behind the wall whose height keeps on decreasing as the wall moves away from it, causing the resultant active force to decrease below the level predicted by the analytical solution that does not accommodate geometric effects. This underscores the advantage of the SPH technique to accommodate geometric effects when the deformation becomes large.

In the passive loading case, the shear band patterns and propagation are more complex than in the active case. From columns (c) and (d) of Figure 2, once again showing ε^p_{acc} and ε_{vol}, initial strain localization occurs around 0.02 m displacement at the bottom left corner by the retaining wall. This initial development is shortly followed by localization in the upper right and left of the backfill, and the initial area of localization at the bottom left corner grows laterally along the bottom of the backfill. After 0.4 m of wall displacement, the regions of strain localization at the top right corner of the wedge extends downwards, and the larger area of localization at the bottom likewise grows upwards. At 0.65 m wall displacement, both areas of localization merge and the band is fully traced, and then by 0.8 m displacement the band thins to form a refined curved band ranging from the bottom left to the top right band of the backfill. At the top left corner, a secondary highly diffuse band begins to form, but never fully propagates downward to the bottom. The geometry and the propagation mechanism of the shear bands from the simulations performed in `GEOSPH` are again very similar to those documented in other studies, although the secondary shear band originating in the top left corner is generally more resolved [64,97]. For further comparison, in the results of Borja and Lai [16], localization is first achieved after 0.05 m of wall displacement, and the shear band was fully traced after 0.2 m of wall displacement.

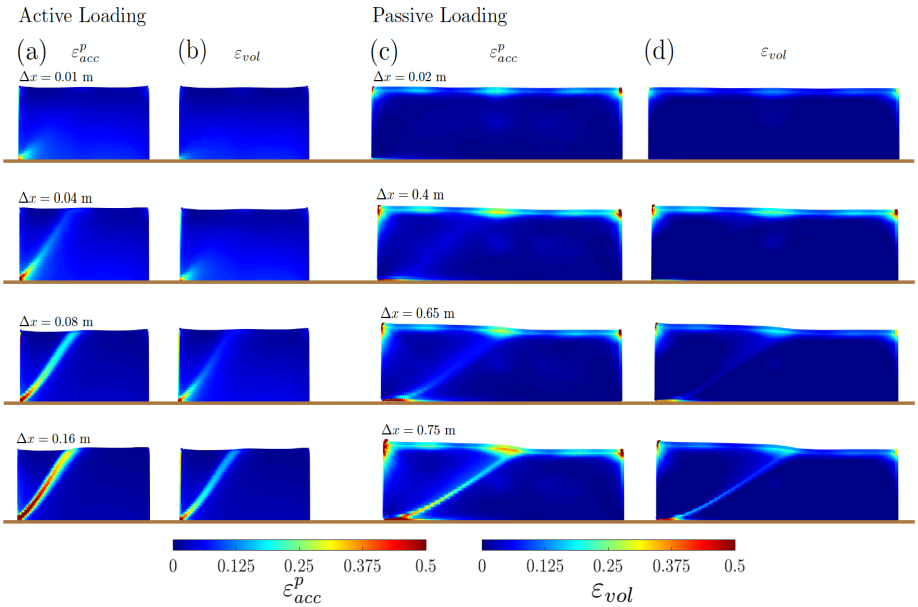

Fig. 2: Shear band development in the actively and passively loaded backfill behind a retaining wall. In columns (a) and (c) the accumulated plastic strain ε^p_{acc} is displayed, while in columns (b) and (d) the volumetric strain ε_{vol} is shown.

In the passive force-displacement curves of Figure 4, the horizontal and vertical forces on the wall rapidly increase as the wall compresses the backfill (panels (a) and (b)), after which the rate decreases as the shear band is fully traced. Like in the active case, however, a residual state and its associated plateau do not occur. Instead, the normal passive force slightly overshoots the NAVFAC solution, while the vertical component of the force undershoots it. Once again, this is due to geometric effects as the effective height of the wedge now increases with increasing horizontal compression, allowing the SPH solution to more realistically predict the horizontal passive force. As for the vertical component of the force, we recall that the NAVFAC solution assumes that the full wall-to-soil friction angle δ has developed behind the wall. This may not necessarily be the case at points close to the base of the wall, where the vertical relative movement between the soil and the wall is much smaller than near the top. It may therefore be argued that the NAVFAC solution likely overpredicts the vertical component of the force, while the SPH solution more realistically captures it. It is also evident that the amount of wall movement necessary to fully trace the failure surface is larger for the passive case than for the active active, which is in agreement with the results from the Terzaghi and Princeton tests as reported by NAVFAC in their Figure 1 on page 7.2-60 [29].

Although the shear bands possess a considerable amount of curvature, resembling a log spiral, and the residual state is never achieved, the orientation of

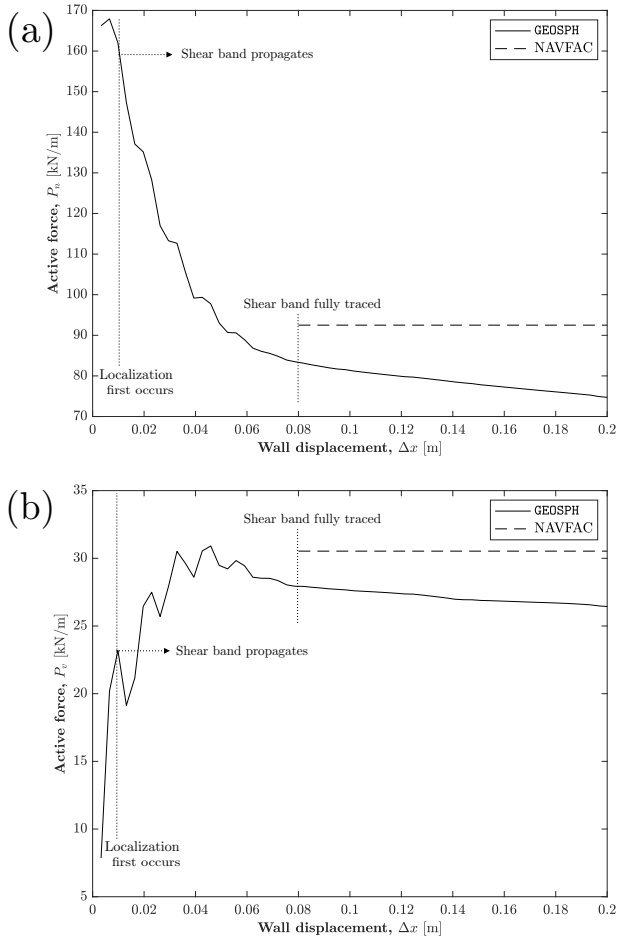

Fig. 3: Force-displacement curves from the retaining wall problem for the active loading case. Panel (a) shows the normal component of the active force P_n, and panel (b) the vertical component P_v.

the shear band at the surface can still be compared with the Arthur, Roscoe, and Coulomb predictions. When the band is fully traced, in the active case at $\Delta x = 0.16$ m, the orientation of the shear band is $\Theta = 53.1^\circ$, a value closest to the Arthur angle $\Theta_A = 53.43^\circ$ for the material parameters of the backfill. In the passive case at $\Delta x = 0.8$ m, the band takes the orientation of $\Theta = 36.2^\circ$, which is also closest to the Arthur angle of $\Theta_A = 36.58^\circ$. Similar agreement of the shear band orientations with the Arthur angle was reported in the work of Borja and Lai [16], which also treated the backfill as an elastoplastic material and made use of the Drucker-Prager yield criterion. This result and the agreement of the shear band patterns with other modeling efforts gives confidence in `GEOSPH`'s capacity to accurately simulate important details of shear band formation in a backfill behind

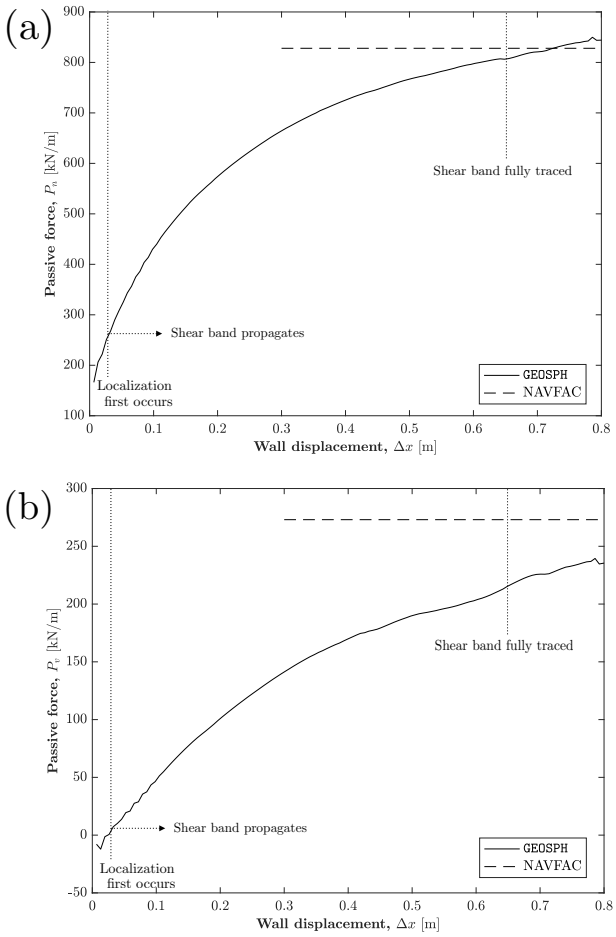

Fig. 4: Force-displacement curves from the retaining wall problem for the passive loading case. Panel (a) shows the normal component of the passive force P_n, and panel (b) the vertical component P_v.

a retaining wall, and motivates the application of the model for more complicated loading scenarios such as the ones described in the next section.

5 Fault propagation problem

5.1 Overview of GEOSPH simulations

The model setup, boundary conditions, and parameters selected (see Table 2 and Figure 5) for the fault propagation simulations performed with GEOSPH are based on the studies of Egholm et al. [31], Finch et al. [37], and Loukidis et al. [59],

among others. The model dimensions given in Table 2 and illustrated in Figure 5 in the extensional and contractional simulations are the same.

In Figure 5, a few important features of the fault propagation problem are highlighted. The synthetic shear band is the primary band forming in the weak overlying material as a result of slip along the blind fault, propagating from the tip of the blind fault and pointing in the same direction. The antithetic band, is conjugate to the synthetic band, and points in the direction opposite to the synthetic band and the blind fault and propagates from the intersection of the blind fault and the hanging wall base. Lastly, the angle of the blind fault in the basement rock is given by θ. Because synthetic shear bands usually do not follow a straight trajectory through the weak overlying sediment material, the angle of orientation of the synthetic band will vary with depth. We consider the shear band angle at the point of surface rupture Θ, or, alternatively, measure the ratio s/p where s is the distance from the fault axis (i.e., the vertical projection of the fault trace) to the point where the synthetic band reaches the surface, and p is the distance from the fault axis to the point where a straight projection of the blind fault would have reached the surface. Thus, the ratio s/p quantifies the deviation from the straight line projection of the shear band.

Table 2: Simulation parameters for the fault propagation experiments.

Parameter	**Value**
Density, ρ [kg/m^3]	1800
Particle mass, m [kg]	1800
Time step, Δt [s]	0.002
Final fault slip, d [m]	12 or 24
Initial inter-particle distance, Δ [m]	1
Smoothing length factor, k_h	1.5
Poisson Ratio, ν	0.3
Young's Modulus, E [kPa]	20,160
Artificial viscosity parameters, α_π and β_π	0.2 and 0.4
Artificial stress parameter, ϵ	0.2
Cohesion, c [kPa]	0 and 100
Internal friction angle, ϕ [°]	30
Dilation angle, ψ [°]	0 and 11
Blind fault dip angle, θ [°]	30, 45, 60
Pushing or pulling velocity, V [m/s]	0.01
Height, H [m]	40
Length, l [m]	150

In total, 18 simulations are conducted (9 extensional and 9 contractional) using `GEOSPH` where the dip angle of the blind fault θ takes the values of 30, 45 and 60°, the angle of internal friction of the weak overlying material is $\phi = 30°$, cohesion is either 0 or 100 kPa, and the angle of dilation ψ is either 0 or 11°. For purposes of clarity we divide our simulations into three groups. The cohesionless simulations, i.e., those which have $c = 0$ kPa and $\psi = 0°$, the cohesional simulations, those which have $c = 100$ kPa and $\psi = 0°$, and the dilational simulations, those with $c = 0$ kPa and $\psi = 11°$. With these three groups of simulations, we can isolate the effects of cohesion and the dilation angle on the behavior of fault propagation or surface rupture in our simulations. The material parameters summarized in Table 2 are selected such that they represent a stiff clay or sand typical of the

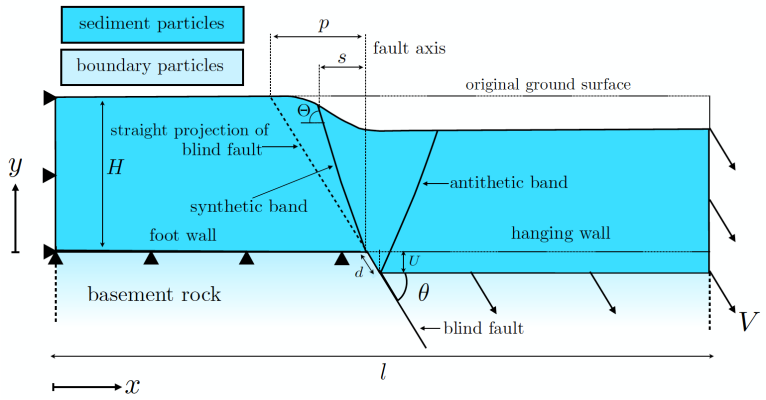

Fig. 5: Boundary value problem setup for the fault propagation problem, here showing the extensional case (contractional one is similar, except V points in the opposite direction). For the overlying weak rock or sediment layer, sediment particles are used, while for the basement and side boundaries, boundary particles are used. One side of the problem boundary (hanging wall) is pulled/pushed by a velocity V, while the other half (foot wall) is fixed.

material overlying a blind fault, and are in line with most characterizations of Mohr-Coulomb parameters for stiff clays at shallow depth [4,59,87].

5.2 Fault propagation mechanism

In all experiments, both extensional and contractional, and regardless of the dip angle of the blind fault θ, strain localization occurs at the sharp corner of the protruding base caused by the slip of the blind fault and then propagates upwards with increasing slip, forming a shear band. In Figure 6, the propagation of the shear band is shown at various intervals of fault slip for the cohesionless $\theta = 30°$ contractional case. In general, the synthetic band forms first, and is followed by the antithetic band (if it forms). In the weak material layer above the basement rock, the pressure field (Figure 7 (a)) increases with depth following the lithostatic gradient, but the deviatoric stress q (Figure 7 (b)) is highest in the area where the shear band originates. In this region, a counterclockwise rotation of the maximum principal stress is observed around the area of strain localization (see Figure 7). A similar rotation is commonly observed in faults in the field, and was similarly reported in the FEM modelling work of Nollet et al. [65]. The analytical solution of Patton and Fletcher [66] based purely on elasticity, also describes a rotation of orientations of the principal stresses depending on the direction of shear in the blind fault, and the orientation of the blind fault itself.

The amount of slip required for the shear band to reach the surface, or, alternatively, for the fault to rupture at the surface, is known as the critical slip d_{cr}. From columns (b) and (c) of Figure 6 depicting the accumulated plastic strain ε^p_{acc} and the volumetric strain ε_{vol}, respectively, the shear band is seen to reach

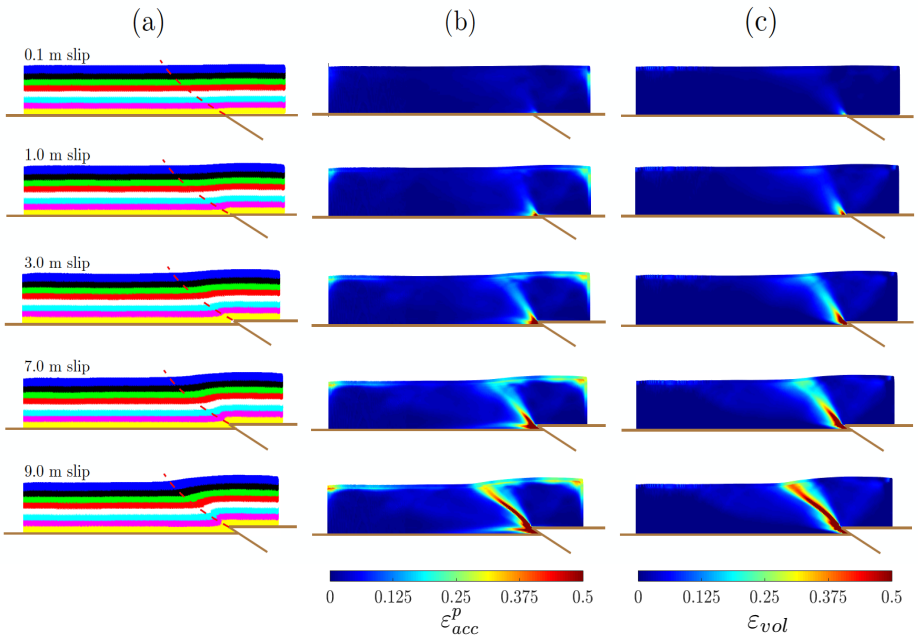

Fig. 6: Shear band initiation in the contractional $\theta = 30°$ cohesionless simulations. Column (a) shows colored material layers to highlight folding and deformation, these otherwise carry no mechanical significance. Cole and Lade [27] failure surfaces are shown superimposed on the colored material layers as dashed red lines. Columns (b) and (c) display ε^p_{acc} and ε_{vol} respectively.

the surface after $d_{cr} = 1.0$ m slip. In Figure 8, the critical slips d_{cr} normalized by the height of the overlying weak layer H, are plotted for the various blind fault angles θ in the contractional and extensional cases for series of simulations varying cohesion and the angle of dilation. The contractional simulations require a greater slip for the shear band to rupture at the surface, and the steeper θ, the larger d_{cr}, with this trend exaggerated for the contractional case. Our results are compared against those of Loukidis et al. [59] and Thebian et al. [87], who used the commercial finite difference (FLAC) and finite element (Abaqus) software for their respective studies, an elastoplastic constitutive model, the Mohr-Coulomb yield criterion, and similar parameters for the overlying weak material layer. The SPH simulations of `GEOSPH` with $c = 100$ kPa match closest to the dense and over-consolidated (bottom of the gray envelope for Loukidis et al.) soil simulations of Thebian et al. and Loukidis et al., which included greater density and cohesion, whereas the $c = 0$ kPa matched closer to the loose simulations (top of the gray envelope for Loukidis et al.).

The orientation of shear bands in the fault propagation problem is a topic of some uncertainty, as studies have demonstrated a degree of disagreement over the shape of the shear bands in the overlying material layer, as well as what parameters control the shape itself and its orientation. From a practical perspective in the

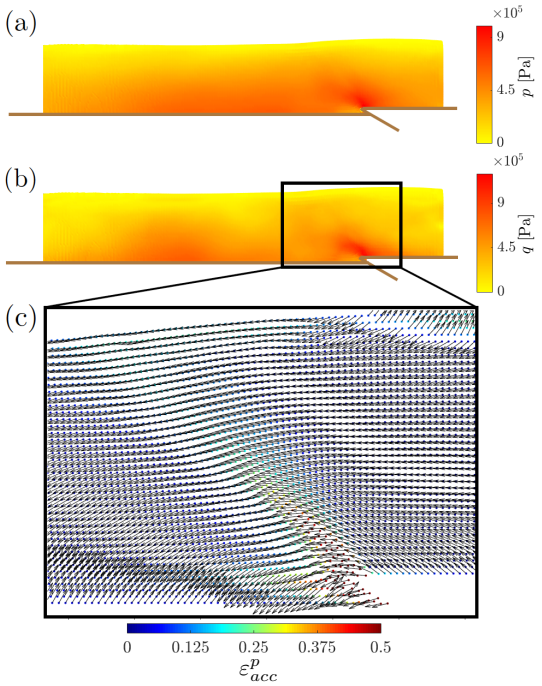

Fig. 7: In panel (a) the pressure field p and in panel (b) the deviatoric stress field q are shown for the cohesionless $\theta = 30^\circ$ simulations at 7 m slip. In panel (c) the directions of the maximum principal stress σ_1 are superimposed over contours of ε^p_{acc} for an augmented region around the shear band.

context of fault propagation, predicting the location of shear band surface rupture in the weak material layer is useful as it is here that most damage occurs [4, 51]. Conversely, observed surface rupture points or scarps could be used to map previously unidentified blind faults at shallow depth, which might otherwise be undetectable using reflection seismic profiles or with other similar geophysics tools.

Similar to the retaining wall problem, under active (extensional) or passive (contractional) conditions, a theoretical prediction for the orientation of the shear band with respect to σ_1 can be found from the Coulomb θ_C, Arthur θ_A or Roscoe θ_R angles. In the fault propagation problem setup however, as seen from Figure 7 (c), the stress field and the directions of σ_1 are significantly distorted by the sharp corners of the blind fault since the loading is not purely in the horizontal direction like in the retaining wall problem. Thus, the Coulomb, Arthur, and Roscoe expressions can only be used to predict the orientation of the shear band at the location of surface rupture, as it is here that σ_1 is parallel to the surface. Even then, past work has found that the angle θ of the blind fault plays a major role in determining the angle of the shear band at the surface. The studies by Finch et al. [36,37] for contractional and extensional simulations, respectively, arrived at this same conclusion, but because their DEM method was only cohesional, and ignored the effects of ϕ, their results were challenged in other subsequent studies [31]. More

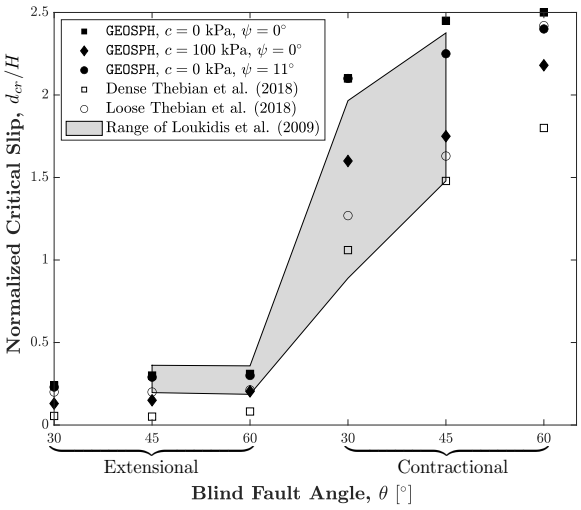

Fig. 8: The normalized critical slip d_{cr}/H required for the shear band ruptures at the surface is plotted against the blind fault angle θ, for our GEOSPH simulations, as well as for the Abaqus results of Thebian et al. [87] and FLAC results of Loukidis et al. [59].

recent versions of the same DEM code now accounting for internal friction have yielded similar results, however [42]. Other modeling efforts using the commercial FEM software Eflen [76], for example, have indicated that the angle of the blind fault plays a key role in the orientation of shear bands, especially as they mature past their initial formation [65]. On the other hand, the work of Egholm et al., [31] found that regardless of the blind fault angle θ, the orientation of the propagating shear bands was always within $\pm 5°$ of the Coulomb predictions, and thus concluded that the angle of internal friction of the weak layer was the controlling parameter.

Lastly, a number of studies have found the Roscoe angle to be the closest match to the orientation of the emergent synthetic shear bands in both extensional and contractional fault propagation experiments, using a combination of analogue sandbox experiments, DEM simulations, and FEM simulations [27,45,51]. Considering the simulations performed with GEOSPH using $c = 0$ kPa and $\psi = 0°$, the expected Coulomb, Roscoe, and Arthur angles are: $\Theta_C = 60°$, $\Theta_R = 45°$, and $\Theta_A = 52.5°$ in extension, and $\Theta_C = 30°$, $\Theta_R = 45°$, and $\Theta_A = 37.5°$ in the contractional case. In Figure 9, these expressions for the shear band angle at the surface rupture point are compared against our GEOSPH simulation results at different slips of the blind fault (quantified as $U = \%H$ for comparison with values reported in the literature, where $U = d \sin\theta$ is the vertical component of slip, see Figure 5).

From Figure 9 we find that the shear band orientation angle is not fixed at a specific value throughout the contraction or extension of the system, but rather varies between all three angle predictions. When the shear band reaches the surface and until $U = 10\%H$, the band is closest to the Roscoe angle, but shortly after

by $U = 15\%H$, has achieved an orientation close to that of the Arthur angle. The shear band spends the majority of time at this orientation until much larger slips are achieved, and around a value of $U = 60\%H$, values closer to slips observed in geological structures such as fault propagation folds, synclines, etc., as opposed to geotechnical scale fault propagation, the shear band reaches an orientation closest to the Coulomb angle. Furthermore, the angle of the blind fault θ evidently plays a role in the final shear band angle sustained at the point of surface rupture. In general, the shear band angle tends to increase with larger θ in extension and smaller θ in contraction.

Given the variability in shear band angle during the temporal evolution of a shear band, and along its length, another measure to quantify and help predict the location of surface rupture or the entire shear band trajectory given a known blind fault would be more valuable. Cole and Lade [27] determined an empirical expression for the propagation path and location of fault surface rupture above a blind fault, making use of the Roscoe angle and expressing the failure surface as a log spiral curve. The propagation paths are always log spirals with their center and orientation depending on the value of θ with respect to the Roscoe angle $\Theta_R = 45^\circ \pm \psi/2$, with the exception of the case where $\theta = \Theta_R$, where the pole of the log spiral is at infinity, rendering a surface which is a straight line. In contraction, and for $\theta = 45^\circ$, the Roscoe angle Θ_R is also 45° since $\psi = 0^\circ$. Hence, the predicted failure surface is a straight line. Cole and Lade's expression also predicts the formation of antithetic bands or faults for $0 \leq \theta < 45 - \psi/2$ in extension, which are a straight line and are oriented at $45^\circ - \psi/2$ from the vertical.

Cole and Lade [27] evaluated their empirical failure surfaces against analogue sandbox-style experiments after small slips d, specifically at $U = 4\%H$, but did not specify how their empirical failure surface changes with increasing slip on the blind fault, or how the same log spiral failure surface performs against actual failure surfaces from experiments at larger slips in the geological range of interest. Looking at Figure 6 (a), the Cole and Lade failure surface does not capture the trajectory of the shear band before surface rupture, or even once the initial surface rupture is reached. It is not until 9.0 m slip is achieved, equivalent to $U = 11.25\%H$, that the Cole and Lade surface actually predicts the surface rupture point observed in the `GEOSPH` simulation for $\theta = 30^\circ$. Looking at Figure 12 column (a) for $\theta = 30^\circ$ at 12 m slip the Cole and Lade log spiral failure surface continues to be a quite accurate prediction of the simulated shear band, but by 24 m slip, ceases to be so, and is inclined too steeply with respect to the horizontal.

Overall, for the different basal angles θ considered in our contractional simulations (see Figure 12), we find that the Cole and Lade empirical log spiral surface captures the location of fault surface rupture s quite accurately for moderate amounts of slip (9 to 12 m slip). In the extensional case (see Figure 11) the Cole and Lade surfaces again predict the location of surface rupture accurately for 9 to 12 m slip, but for greater slip, the shear bands curve away from the log spiral surface. In general, the log spiral shape of the failure surfaces does not match the curvature of the shear bands for some blind fault angles, most notably $\theta = 30^\circ$ in the contractional simulations, and in the extensional simulations for the principal synthetic band. Good agreement in the surface rupture locations, but discrepancies in the fault curvature with respect to the empirical solutions, was also reported in the DEM simulations of Garcia and Bray [38], and Hazeghian and Soroush [46]. Most notably, in both `GEOSPH` and DEM simulations, the shear bands have much

straighter paths, experiencing a smaller amount of curvature between the point of nucleation and of surface rupture than that predicted by the log spiral curves.

On the other hand, the antithetic shear bands which only reliably form in the extensional case, have a less variable orientation angle Θ at the surface than do the synthetic bands, and have values close to the Arthur angle. Interestingly, the angle of the blind fault θ does not significantly affect the antithetic shear band angle either, suggesting that the horizontal rather than vertical loading conditions dominate in the hanging wall of the extensional normal fault setup, similar to the retaining wall problem, thus also resulting in an Arthur angle shear band orientation. The insensitivity of the orientation of the antithetic bands to the blind fault angle was also observed by Egholm et al [31] and Nollet et al. [65]. Because the empirical relations of Cole and Lade [27] predict a straight band with the orientation given by the Roscoe angle, they do not agree with the mostly straight bands generated by `GEOSPH` at the Arthur angle.

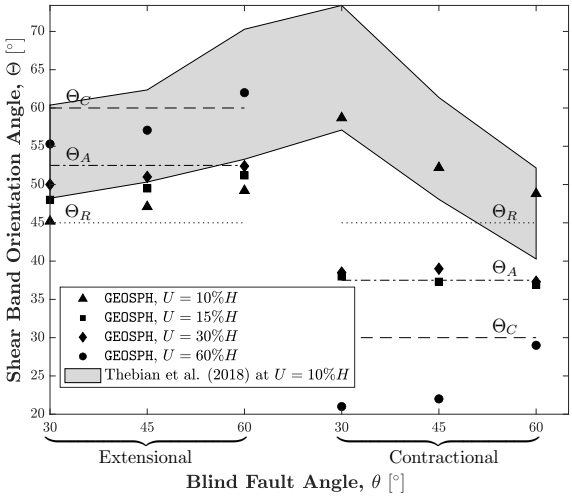

Fig. 9: The shear band orientations with respect to the horizontal at the top surface near the point of surface rupture Θ measured from our `GEOSPH` simulations compared against the results of Thebian et al. [87] and against the Coulomb Θ_C, Arthur Θ_A, and Roscoe Θ_R angle predictions.

Because we see that the shear band propagation process is a dynamic one, and a single angle or failure surface cannot capture the progression of fault surface rupture with increasing slip along the blind fault, we propose using the s/p ratio to quantify the deviation of the shear band from the straight line projection of the blind fault. An s/p ratio of one indicates a shear band that propagates at the same angle of the blind fault. Given an expected amount of slip d, the s/p empirical relation can give the expected outcropping location of fault rupture along the surface for different blind fault angles θ. In Figure 10, the s/p ratio is displayed for the three different simulation groups, cohesionless, cohesional, and dilational, at the three different basal angles for the extensional and contractional

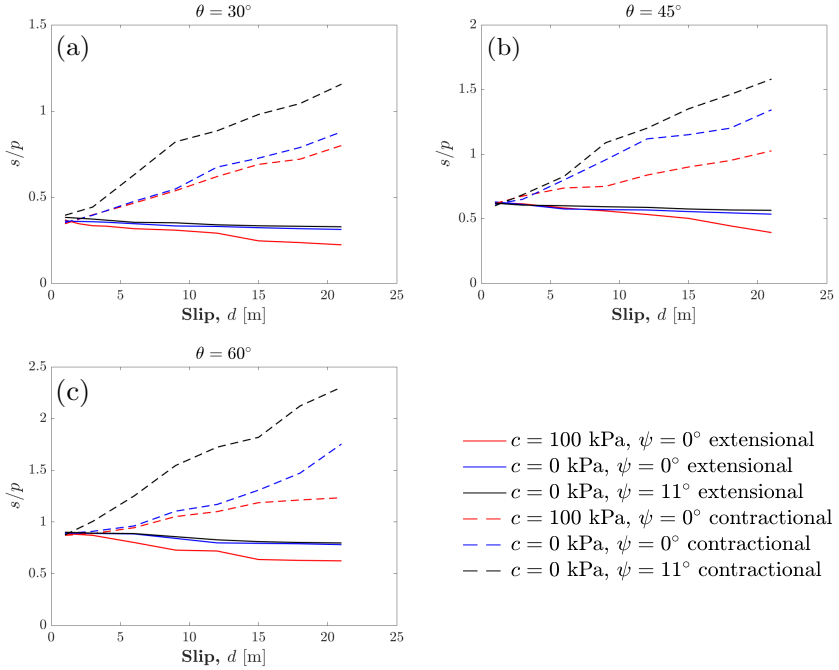

Fig. 10: The s/p ratio for the contractional and extensional cases for all three simulation groups, cohesionless, cohesional, and dilational. In (a) for $\theta = 30°$, in (b) for $\theta = 45°$, in (c) for $\theta = 60°$.

cases. In the extensional case for all three basal angles, the deviation from the straight line projection is smallest (steeper than the straight line projection), and of these, the simulations with $\psi = 11°$ have the least deviation, closely followed by the cohesional simulations with $c = 100$ kPa. In the contractional case, the simulations with $\psi = 11°$ have the greatest deviation, and those with cohesion the least.

5.3 Evaluation of structural styles

Considering our results for the cohesionless extensional case first, in Figure 11, colored material layers or markers are plotted in column (a) at $d = 6$ m and $d = 12$ m slip. In column (b), contours of the accumulated plastic strain ε^p_{acc} are shown, and in column (c) contours of the magnitude of the vertical component of the velocity vector v are displayed. In the $\theta = 30°$ case, a set of conjugate shear bands form with clear synthetic and antithetic bands, forming a graben-horst complex structure. The conjugate bands and graben-horst structure develop with time, becoming fully mature once 12 m slip is reached. For simulations with steeper basement fault angle such as $\theta = 60°$, a graben-horst complex is no longer produced, an antithetic shear band is no longer visible, and instead, a smoother rolling monocline forms. In the $\theta = 45°$ simulations, a transitional state between

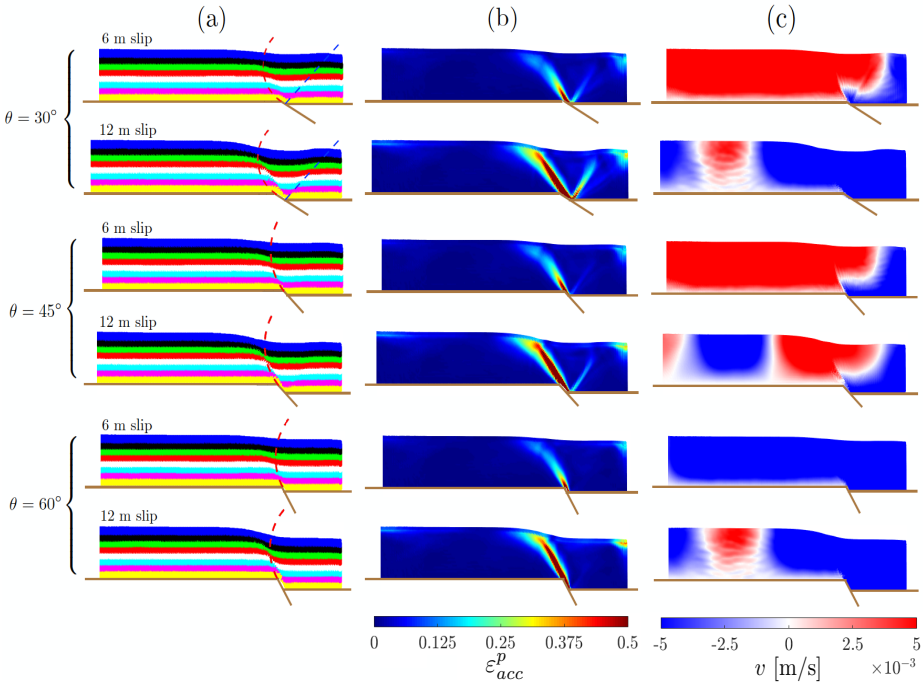

Fig. 11: The cohesionless extensional simulations are shown for varying blind fault angles at 6 and 12 m slip. In column (a) colored material layers are shown alongside the Cole and Lade [27] failure surfaces in dashed red and blue lines. In column (b) and (c), ε^p_{acc} and the vertical component v of velocity are shown, respectively.

a graben-horst complex and a monocline is observed, with a small but visible antithetic shear band forming. After the graben-horst complex forms between 6 and 12 m slip, the graben tends to move upwards along with the foot wall as seen from the vertical velocity plots in column (c) of Figure 11, and only the material behind the antithetical band moves downwards as the system extends, and it is here that the most vertical extension occurs in the overlying material layer. When the graben does not form and there is no antithetic shear band, like in the $\theta = 60^\circ$ case, the entire hanging wall moves vertically downwards, this causes the shear band to rotate vertically, causing a very steep orientation Θ with respect to the horizontal as seen in Figure 9.

In Figure 12 colored material layers are plotted for the contractional equivalent cohesionless simulations, with varying θ at 12 and 24 m slip. A monocline is the dominant geological structure in all three simulations regardless of the blind fault dip angle θ. Overall, for all three different θ simulations, but especially markedly in the $\theta = 60^\circ$ simulation, as slip increases, layer thinning is increasingly evident in the vicinity of the synthetic shear band on the hanging wall while layer thickening occurs close by on the foot wall, as also observed by Finch et al. [36]. Additionally, convex drag folding is observed where the material layers bend away from the direction of band propagation motion.

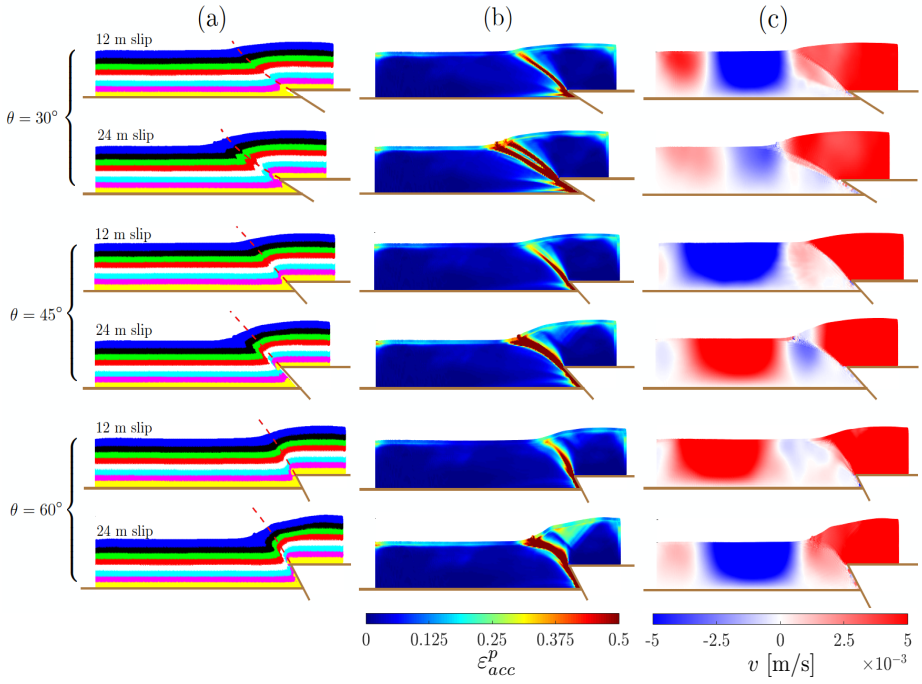

Fig. 12: The cohesionless contractional simulations are shown for varying blind fault angles at 12 and 24 m slip. In column (a) colored material layers are shown alongside the Cole and Lade [27] failure surfaces in dashed red lines. In column (b) and (c), ε^p_{acc} and the vertical component v of velocity are shown, respectively.

Drag folding is a common feature found in reverse faults in the field and has been observed in multiple numerical studies of contractional reverse faults [36, 75]. In the colored material layers at 24 m slip, the bottom few layers deform beyond drag folding and a kinematic discontinuity across the shear band or fault plane is visible, as the previously connected yellow and magenta colored layers are severed. This result shows how material rupture and kinematic discontinuities arise in SPH given sufficiently large levels of deformation. From column (c) of Figure 12, we see that the entirety of the hanging wall experiences upward vertical motion, while the immediate foot wall is mostly stationary. At some distance from the band along the top surface of the foot wall, a surface depression is recorded with downward vertical motion (see also Figure 17) in most θ cases. Our simulation results produced by `GEOSPH` in both the extensional and contractional case closely resemble reported results by similar studies using FEM, DEM, or analogue sandbox experiments [6,31,36,37,45,59,65], especially in terms of the overall geological structures produced at different blind fault dips θ.

In Figure 13, extensional and contractional simulations with either $c = 100$ kPa (cohesional) or $\psi = 11°$ (dilational) are plotted to consider the effect of cohesion or varying the dilation angle to our fault propagation simulations. In extension, cohesion helps stabilize the steeper surface slopes associated with the

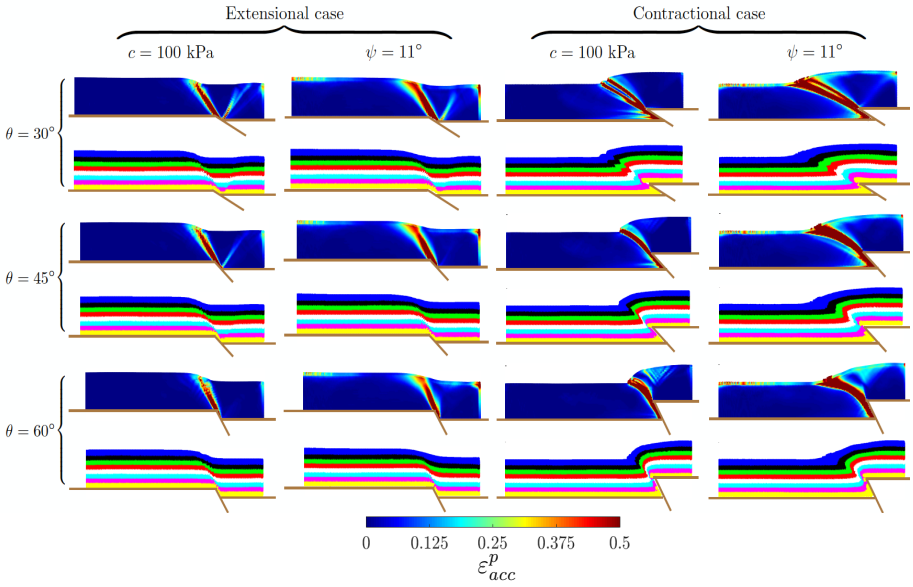

Fig. 13: The accumulated plastic strain ε^p_{acc} and colored material layers are shown for all different simulation types with the cohesional ($c = 100$ kPa, $\psi = 0°$) and dilational ($c = 0$ kPa, $\psi = 11°$) materials at 12 m slip for the extensional simulations and 24 m slip for the contractional simulations.

fold between the horst and graben, whereas increasing the angle of dilation leads the horsts to collapse under gravity, smoothing out the topographic surface. Like in the extensional case, the addition of cohesion in the contractional case serves to steepen the overall monocline and reduces the degree to which the shear bands bend away from the straight propagation line of the blind fault (this bending is measured in Figure 10 with the s/p ratio). Increasing the dilation angle once again has the opposite effect.

5.4 Deformed surface profiles

We have seen that qualitatively our results for the fault propagation problem match the structural styles described in the modeling literature and in the field. However, in order to more rigorously determine whether `GEOSPH` along with our elastoplastic soil behavior was capable of replicating realistic fault propagation behavior and associated surface uplift and deformation, we validate the amount of surface uplift recorded from some of our simulations against that from the centrifuge experiments of Bransby et al. [20,21]. Bransby et al. conducted fault propagation experiments with a similar setup to those performed in this study for the contractional and extensional cases, using dry cohesionless Fontainebleau sand, with density and angle of friction similar to that selected in our simulation input parameters, and a blind fault angle of $\theta = 60°$. In Figure 14 we compare the normalized surface displacement $\Delta y/H$ produced by `GEOSPH` against the contractional reverse faulting

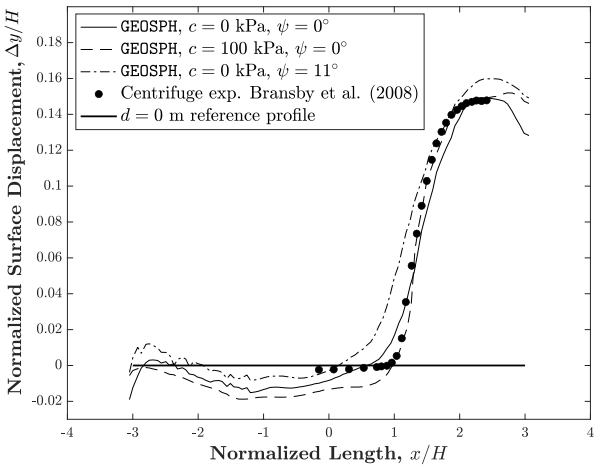

Fig. 14: Normalized surface displacement for the cohesionless, cohesional, and dilational GEOSPH simulations compared against that from the centrifuge experiments of Bransby et al. [21] in the contractional case.

experiments reported in [21], and in Figure 15 against the extensional normal faulting reported in [20] at $U = 14.7\%H$ and $U = 8.6\%H$, respectively. Specifically, we consider the three different groups of simulations performed with GEOSPH: those with $c = 0$ kPa and $\psi = 0°$, those with $c = 100$ kPa and $\psi = 11°$, and lastly, those with $c = 0$ kPa and $\psi = 11°$.

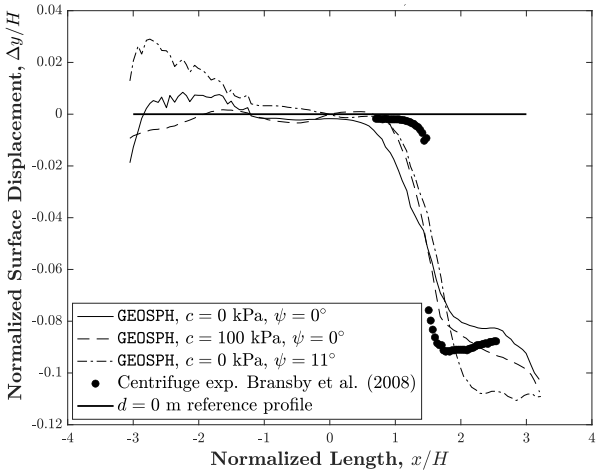

Fig. 15: Normalized surface displacement for the cohesionless, cohesional, and dilational GEOSPH simulations compared against that from the centrifuge experiments of Bransby et al. [20] in the extensional case.

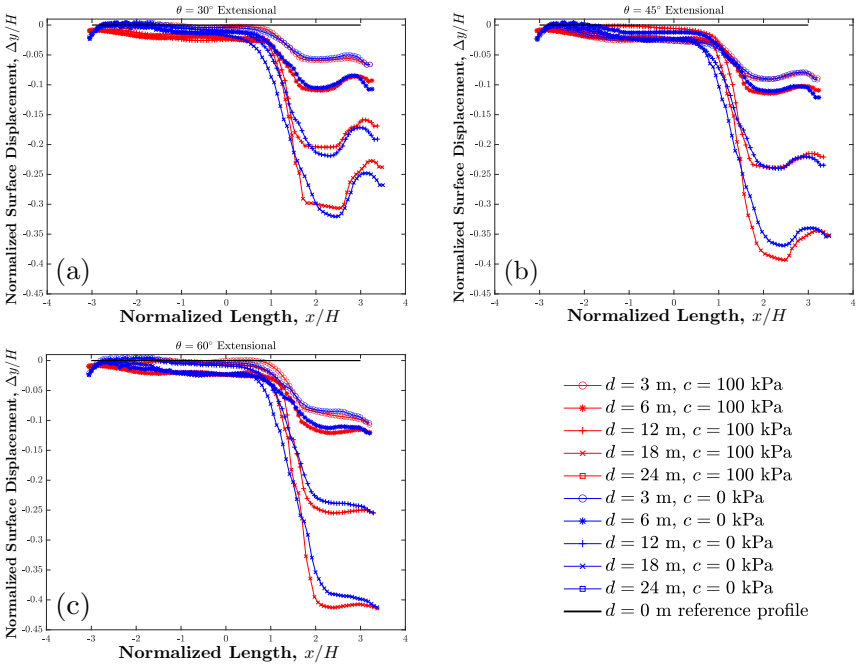

Fig. 16: Normalized surface displacement profiles for the cohesional and cohesionless simulations at different slips for the extensional simulations. In panel (a) the $\theta = 30^\circ$ case, in (b) the $\theta = 45^\circ$, and in (c) the $\theta = 60^\circ$.

There is strong agreement between the contractional experiments of Bransby et al. and the cohesionless $c = 0$ kPa and $\psi = 0^\circ$ and the cohesional $c = 100$ kPa and $\psi = 0^\circ$ simulation results. The cohesional simulation captures the top profile of the monocline remarkably well, as well as the steep slope, but the cohesionless simulation predicts a reduced depression at the bottom of the monocline, which is closer to that reported in the centrifuge experiments. The dilational $c = 0$ kPa and $\psi = 11^\circ$ simulation does not fit the experimental centrifuge data particularly well, its topographic slope is less steep, and the scarp has excessive height. In the extensional case, the elevations or $\Delta y/H$ for the monoclines are correctly reproduced by `GEOSPH`, but the slope of the monocline is far greater in the centrifuge experiments than in any simulations produced by `GEOSPH`. This fact is responsible for the visible offset between the data sets. The shallower surface slopes of the `GEOSPH` simulations may be due to the known tendency for SPH to over-smooth material properties near boundaries and free surfaces [33]. From both contractional and extensional cases, we note that the dilational simulations approximate the centrifuge experiments of Bransby et al. the worst. Thus, having validated our fault propagation surface profiles against the results of Bransby et al. with a considerable degree of confidence, we proceed to consider the additional case of $\theta = 30$ and 45°, in both extensional and contractional cases as well as the temporal evolution of surface profiles solely for the cohesional and cohesionless simulation groups.

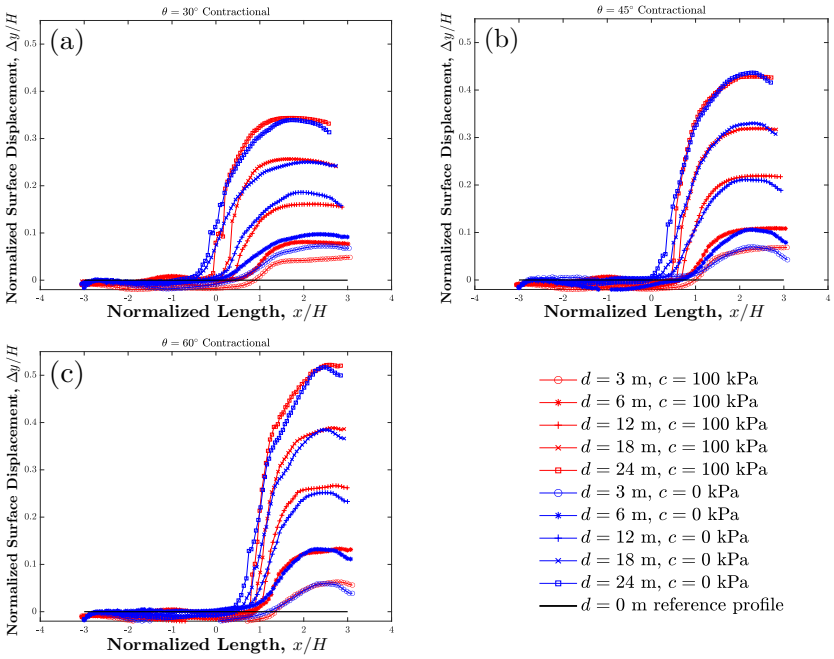

Fig. 17: Normalized surface displacement profiles for the cohesional and cohesionless simulations at different slips for the contractional simulations. In panel (a) the $\theta = 30^\circ$ case, in (b) the $\theta = 45^\circ$, and in (c) the $\theta = 60^\circ$.

In Figure 16 the normalized surface displacement profiles are plotted against the normalized length for the extensional case at different amounts of slip for the cohesional and cohesionless simulation groups at the three different blind fault angles. Similarly, in Figure 17 the same plots are recreated for the contractional case. Simulations with $\theta = 60^\circ$ result in the greatest amount of vertical surface displacement in both extensional and contractional simulations, with a total depression in the extensional case of close to $\Delta y = -45\%H$ and a total elevation gain of $\Delta y = 39\%H$ in the contractional case for slippage of $d = 12$ m. For low slip, cohesional simulations have slightly less surface displacement change than cohesionless ones, although this trend is reversed for greater slip (generally above $d = 6$ m). In some of these cases for greater slip, cohesionless simulations will eventually reach the same maximum surface change as cohesional ones, but only after some sufficient extra distance x, as the cohesionless surface slopes are shallower. The steeper slopes resulting from surface elevation change caused by propagating faults in cohesional soils as opposed to cohesionless soils clearly pose an increased risk to any overlying structures.

6 Closure

In this paper we implement `GEOSPH`, a meshfree fully Lagrangian smoothed particle hydrodynamics (SPH) code, to handle the large deformation of elastoplastic geomaterials, and study the patterns and geometry of strain localization phenomena and faulting in two distinct set of problems: an actively and a passively loaded backfill behind a retaining wall, and the propagation of a blind fault across a weak overlying medium. To the best knowledge of the authors, this paper represents the first time SPH has been used to study both of these problems. We show that in `GEOSPH`, shear bands arise naturally without the need for a heterogeneity or seed to trigger their formation, and that the SPH method can accurately model problems where external loadings are applied in addition to gravitational loads. Our results show that shear band orientation varies according to boundary conditions and the level of deformation. We find shear bands oriented at the Arthur angle with respect to the horizontal at the top of the backfill, and in the fault propagation problem, for fault displacements between $U = 15$ to $60\%H$, the orientation of the band at the surface is also given by the Arthur angle, and is preceded by the Roscoe orientation and succeeded by the Coulomb orientation. We also observe that the particular blind fault angle in both extensional and contractional cases moderately affects the orientation of the propagating shear band, agreeing with previous studies [36,37]. Furthermore, we find that the failure surfaces of Cole and Lade [27] are accurate for small fault displacements close to the one used in their original study, but for larges slips, especially for those observed in basins in structural geology, the empirical surfaces are inaccurate.

In terms of the critical slip required for the shear band to propagate to the surface d_{cr}, the contractional simulations require a larger amount of slip than the extensional ones for the shear band to rupture at the surface, and the larger the blind fault angle, the larger d_{cr}. Our simulations also capture a variety of geological phenomena occurring in the vicinity of the propagating faults, most notably layer thinning or thickening and drag folding, and even kinematic discontinuities across the faults. In the extensional case, we observe that graben-horst complexes form in systems with shallower blind fault angles, whereas those with steeper blind fault angles do not form grabens. In the contractional simulations, no grabens are produced, and a sole monocline forms. Regarding the effects of different material parameters on our simulation results, we deduce that the dilation angle ψ helps to increase the curvature or the amount of offset from the straight line propagation of the fault, while cohesion c has the opposite effect. In fact cohesion helps produce greater surface displacement and steeper surface slopes at the fault rupture point.

In our study we focused on shear band and fault propagation in elastic-perfectly plastic geomaterials. Future work will include an exploration of the effects of strain hardening or softening behavior on shear band patterns and propagation mechanisms, or how these properties vary with different features of the constitutive models, such as anisotropy [81,104,105], viscoelasticity [93], or viscoplasticity [19]. An exploration of the factors controlling the width and intensity of shear bands, not just their orientation and propagation direction, would also be worthwhile. From a modeling perspective, considering the effects of foundations or tunnels in the vicinity of a propagating fault would also be interesting problems worthy of tackling with SPH going forward. Incorporation of some of these factors into our models is currently being considered in our work.

Acknowledgements This material is based upon work supported by the U.S. Department of Energy, Office of Science, Office of Basic Energy Sciences, Geosciences Research Program, under Award Number DE-FG02-03ER15454. Support for materials and additional student hours were provided by the National Science Foundation under Award Number CMMI-1914780. The first author acknowledges the support by the U.S. National Science Foundation (NSF) Graduate Research Fellowship under Grant DGE 1656518, as well as by the Stanford Graduate Fellowship.

References

1. Adami, S., Hu, X.Y., Adams, N.A.: A generalized wall boundary condition for smoothed particle hydrodynamics. Journal of Computational Physics **231**, 7057–7075 (2012)
2. Adami, S., Hu, X.Y., Adams, N.A.: A transport-velocity formulation for smoothed particle hydrodynamics. Journal of Computational Physics **241**, 292–307 (2013)
3. Allmendinger, R.W., Shaw, J.: Estimation of fault propagation distance from fold shape: Implications for earthquake hazard assessment. Geology **28**(12), 1099–1102 (2000)
4. Anastasopoulos, I., Gazetas, G.: Foundation-structure systems over a rupturing normal fault: Part II. Analysis of the Kocaeli case histories. Bulletin of Earthquake Engineering **5**, 277–301 (2007)
5. Anastasopoulos, I., Gazetas, G.: Analysis of cut-and-cover tunnels against large tectonic deformation. Bulletin of Earthquake Engineering **8**, 283–307 (2010)
6. Anastasopoulos, I., Gazetas, G., Bransby, M.F., Davies, M.C.R., Nahas, A.E.: Fault rupture propagation through sand: Finite-element analysis and validation through centrifuge experiments. Journal of Geotechnical and Geoenvironmental Engineering **133**(8), 943–958 (2007)
7. Arthur, J.R.F., Dunstan, T., Al-Ani, Q.A.J.L., Assadi, A.: Plastic deformation and failure in granular media. Géotechnique **27**(1), 53–74 (1977)
8. Baziar, M.H., Nabizadeh, A., Lee, C.J., Hung, W.Y.: Centrifuge modeling of interaction between reverse faulting and tunnel. Soil Dynamics and Earthquake Engineering **65**, 151–164 (2014)
9. Belytschko, T., Black, T.: Elastic crack growth in finite elements with minimal remeshing. International Journal for Numerical Methods in Engineering **45**, 601–620 (1999)
10. Bonet, J., Lok, T.S.: Variational and momentum preservation aspects of smooth particle hydrodynamics formulations. Computer Methods in Applied Mechanics and Engineering **180**(1-2), 97–115 (1999)
11. Borja, R.I.: A finite element model for strain localization analysis of strongly discontinuous fields based on standard Galerkin approximation. Computer Methods in Applied Mechanics and Engineering **190**(11-12), 1529–1549 (2000)
12. Borja, R.I.: Bifurcation of elastoplastic solids to shear band mode at finite strain. Computer Methods in Applied Mechanics and Engineering **191**(46), 5287–5314 (2002)
13. Borja, R.I.: Computational modeling of deformation bands in granular media, II: Numerical simulations. Computer Methods in Applied Mechanics and Engineering **193**(27–29), 2699–2718 (2004)
14. Borja, R.I.: Plasticity Modeling & Computation. Springer-Verlag (2013)
15. Borja, R.I., Aydin, A.: Computational modeling of deformation bands in granular media, I: Geological and mathematical framework. Computer Methods in Applied Mechanics and Engineering **193**(27–29), 2667–2698 (2004)
16. Borja, R.I., Lai, T.Y.: Propagation of localization instability under active and passive loading. Journal of Geotechnical and Geoenvironmental Engineering **128**(1), 64–75 (2002)
17. Borja, R.I., Song, X., Rechenmacher, A.L., Abedi, S., Wu, W.: Shear band in sand with spatially varying density. Journal of the Mechanics and Physics of Solids **61**(1), 219–234 (2013)
18. Borja, R.I., Song, X., Wu, W.: Critical state plasticity. Part VII: Triggering a shear band in variably saturated porous media. Computer Methods in Applied Mechanics and Engineering **261-262**, 66–82 (2013)
19. Borja, R.I., Yin, Q., Zhao, Y.: Cam-Clay plasticity. Part IX: On the anisotropy, heterogeneity, and viscoplasticity of shale. Computer Methods in Applied Mechanics and Engineering **360**, 112695 (2020)

20. Bransby, M.F., Davies, M.C.R., Nahas, A.E.: Centrifuge modeling of normal fault-foundation interaction. Bulletin of Earthquake Engineering **6**, 585–605 (2008)
21. Bransby, M.F., Davies, M.C.R., Nahas, A.E., Nagaoka, S.: Centrifuge modeling of reverse fault-foundation interaction. Bulletin of Earthquake Engineering **6**, 607–628 (2008)
22. Bui, H.H., Fukagawa, R.: An improved SPH method for saturated soils and its application to investigate the mechanisms of embankment failure: Case of hydrostatic pore-water pressure. International Journal for Numerical and Analytical Methods in Geomechanics **37**, 31–50 (2013)
23. Bui, H.H., Fukagawa, R., Sako, K., Ohno, S.: Lagrangian meshfree particles method (SPH) for large deformation and failure flows of geomaterial using elastic–plastic soil constitutive model. International Journal for Numerical and Analytical Methods in Geomechanics **32**, 1537–1570 (2008)
24. Bui, H.H., Fukagawa, R., Sako, K., Wells, J.C.: Slope stability analysis and discontinuous slope failure simulation by elasto-plastic smoothed particle hydrodynamics (SPH). Géotechnique **61**(7), 565–574 (2011)
25. Caquot, A., Kerisel, J.: Tables for the Calculation of Passive Pressure, Active Pressure and Bearing Capacity of Foundations. Gauthier-Villars, Paris (1948)
26. Colagrossi, A., Bouscasse, B., Antuono, M., Marrone, S.: Particle packing algorithm for SPH schemes. Computer Physics Communications **183**(8), 1641–1653 (2012). DOI https://doi.org/10.1016/j.cpc.2012.02.032. URL http://www.sciencedirect.com/science/article/pii/S0010465512001051
27. Cole, D.A., Lade, P.V.: Influence zones in alluvium over dip-slip faults. Journal of Geotechnical Engineering **110**(5), 599–615 (1984)
28. Coulomb, C.A.: Essai sur une application des regles des maximis et minimis a quelques problemes de statique relatifs a l'architecture. Memoires de l'Academie Royale pres Divers Savants **7** (1776)
29. Design Manual 7.02: Foundations and Earth Structures: Naval Facilities Engineering Command (1986)
30. Desrues, J., Argilaga, A., Caillerie, D., Combe, G., Nguyen, T.K., Richefeu, V., Pont, S.: From discrete to continuum modelling of boundary value problems in geomechanics: An integrated FEM-DEM approach. International Journal for Numerical and Analytical Methods in Geomechanics **43**(5), 919–955 (2019)
31. Egholm, D.L., Sandiford, M., Clausen, O.R., Nielsen, S.B.: A new strategy for discrete element numerical models: 2. Sandbox applications. Journal of Geophysical Research **112**, B05204 (2007)
32. Erslev, E.: Trishear fault-propagation folding. Geology **19**(6), 617–620 (1991)
33. Fávero Neto, A.H.: A continuum Lagrangian finite deformation computational framework for modeling granular flows. Ph.D. thesis, Stanford University (2020)
34. Fávero Neto, A.H., Askarinejad, A., Springman, S.M., Borja, R.I.: Simulation of debris flow on an instrumented test slope using an updated Lagrangian particle method. Acta Geotechnica **15**, 2757–2777 (2020)
35. Fávero Neto, A.H., Borja, R.I.: Continuum hydrodynamics of dry granular flows employing multiplicative elastoplasticity. Acta Geotechnica **13**(5), 1027–1040 (2018)
36. Finch, E., Hardy, S., Gawthorpe, R.: Discrete element modelling of contractional fault-propagation folding above rigid basement fault blocks. Journal of Structural Geology **25**(4), 518–528 (2003)
37. Finch, E., Hardy, S., Gawthorpe, R.: Discrete-element modelling of extensional fault-propagation folding above rigid basement fault blocks. Basin Research **16**, 489–506 (2004)
38. Garcia, F.E., Bray, J.D.: Distinct element simulations of shear rupture in dilatant granular media. International Journal of Geomechanics **18**(9), 04018111 (2018)
39. Gingold, R., Monaghan, J.: Smoothed particle hydrodynamics: theory and application to nonspherical stars. Monthly Notices of the Royal Astronomical Society **181**, 375–389 (1977)
40. Gomez-Gesteira, M., Rogers, B.D., Dalrymple, R.A., Crespo, A.J.: State-of-the-art of classical SPH for free-surface flows. Journal of Hydraulic Research **48**(sup1), 6–27 (2010)
41. Gray, J., Monaghan, J., Swift, R.: SPH elastic dynamics. Computer Methods in Applied Mechanics and Engineering **190**(49-50), 6641–6662 (2001)
42. Hardy, S.: Propagation of blind normal faults to the surface in basaltic sequences: Insights from 2D discrete element modelling. Marine and Petroleum Geology **48**, 149–159 (2013)

43. Hardy, S.: Discrete element modelling of extensional, growth, fault-propagation folds. Basin Research **31**, 584–599 (2018)
44. Hardy, S., Finch, E.: Mechanical stratigraphy and the transition from trishear to kink-band fault-propagation fold forms above blind basement thrust faults: A discrete-element study. Marine and Petroleum Geology **24**(2), 75–90 (2007)
45. Hazeghian, M., Soroush, A.: DEM simulation of reverse faulting through sands with the aid of GPU computing. Computers and Geotechnics **66**, 253–263 (2015)
46. Hazeghian, M., Soroush, A.: DEM-aided study of shear band formation in dip-slip faulting through granular soils. Computers and Geotechnics **71**, 221–236 (2016)
47. Hu, Y., Randolph, M.: A practical numerical approach for large deformation problems in soil. International Journal for Numerical and Analytical Methods in Geomechanics **22**(5), 327–350 (1998)
48. Hughes, T., Winget, J.: Finite rotation effects in numerical integration of rate constitutive equations arising in large-deformation analysis. International Journal for Numerical Methods in Engineering **15**(12), 1862–1867 (1980)
49. Jin, Y.F., Yuan, W.H., Yin, Z.Y., Cheng, Y.M.: An edge-based strain smoothing particle finite element method for large deformation problems in geotechnical engineering. International Journal for Numerical and Analytical Methods in Geomechanics **44**(7), 923–941 (2020)
50. Kermani, E., Qiu, T.: Simulation of quasi-static axisymmetric collapse of granular columns using smoothed particle hydrodynamics and discrete element methods. Acta Geotechnica **15**, 423–437 (2020)
51. Lade, P.V., Cole, D.A., Cummings, D.: Multiple failure surfaces over dip-slip faults. Journal of Geotechnical Engineering **110**(5), 616–627 (1984)
52. Li, X., Konietzky, H., Li, X., Wang, Y.: Failure pattern of brittle rock governed by initial microcrack characteristics. Acta Geotechnica **14**, 1437–1457 (2019)
53. Liang, W., Zhao, J.: Multiscale modeling of large deformation in geomechanics. International Journal for Numerical and Analytical Methods in Geomechanics **43**(5), 1080–1114 (2019)
54. Liu, F.: Modeling hydraulic fracture propagation in permeable media with an embedded strong discontinuity approach. International Journal for Numerical and Analytical Methods in Geomechanics **44**(12), 1634–1655 (2020)
55. Liu, F., Borja, R.I.: A contact algorithm for frictional crack propagation with the extended finite element method. International Journal for Numerical and Analytical Methods in Geomechanics **76**, 1489–1512 (2008)
56. Liu, F., Borja, R.I.: Stabilized low-order finite elements for frictional contact with the extended finite element method. Computer Methods in Applied Mechanics and Engineering **199**(37-40), 2456–2471 (2010)
57. Liu, F., Borja, R.I.: Extended finite element framework for fault rupture dynamics including bulk plasticity. International Journal for Numerical and Analytical Methods in Geomechanics **37**(18), 3087–3111 (2013)
58. Liu, G.R., Liu, M.B.: Smoothed Particle Hydrodynamics: A meshfree particle method. World Scientific (2003)
59. Loukidis, D., Bouckovalas, G.D., Papadimitriou, A.G.: Analysis of fault rupture propagation through uniform soil cover. Soil Dynamics and Earthquake Engineering **29**(11-12), 1389–1404 (2009)
60. Lucy, L.B.: A numerical approach to the testing of the fission hypothesis. The Astronomical Journal **82**(12) (1977)
61. Ma, G., Regueiro, R., Zhou, W., Liu, J.: Spatiotemporal analysis of strain localization in dense granular materials. Acta Geotechnica **14**, 973–990 (2019)
62. Mitra, S., Mount, V.: Foreland basement-involved structures. American Association of Petroleum Geologists Bulletin **82**(1), 70–109 (1998)
63. Nguyen, N.H.T., Bui, H.H., Nguyen, G.D.: An approach to calculating large strain accumulation for discrete element simulations of granular media. International Journal for Numerical and Analytical Methods in Geomechanics **44**(11), 1525–1547 (2020)
64. Nitka, M., Tejchman, J., Kozicki, J., Leśniewska, D.: DEM analysis of micro-structural events within granular shear zones under passive earth pressure conditions. Granular Matter **17**, 325–343 (2015)
65. Nollet, S., Vennekate, G.J.K., Giese, S., Vrolijk, P., Urai, J.L., Ziegler, M.: Localization patterns in sandbox-scale numerical experiments above a normalfault in basement. Journal of Structural Geology **39**, 199–209 (2012)

66. Patton, T.L., Fletcher, R.C.: Mathematical block-motion model for deformation of a layer above a buried fault of arbitrary dip and sense of dip. Journal of Structural Geology **17**(10), 1455–1472 (1995)
67. Peng, C., Guo, X., Wu, W., Wang, Y.: Unified modelling of granular media with Smoothed Particle Hydrodynamics. Acta Geotechnica **11**, 1231–1247 (2016)
68. Peng, C., Wang, S., Wu, W., Yu, H., Wang, C., Chen, J.Y.: LOQUAT: an open-source GPU-accelerated SPH solver for geotechnical modeling. Acta Geotechnica **14**, 1269–1287 (2019)
69. Peng, C., Wu, W., Yu, H.S.Y., Wang, C.: A SPH approach for large deformation analysis with hypoplastic constitutive model. Acta Geotechnica **10**, 703–717 (2015)
70. Pollard, D.D., Fletcher, R.C.: Fundamentals of Structural Geology. Cambridge University Press (2005)
71. Pollard, D.D., Martel, S.J.: Structural Geology (A Quantitative Introduction). Cambridge University Press (2020)
72. Ramachandran, P., Bhosale, A., Puri, K., Negi, P., Muta, A., Dinesh, A., Menon, D., Govind, R., Sanka, S., Sebastian, A.S., Sen, A., Kaushik, R., Kumar, A., Kurapati, V., Patil, M., Tavker, D., Pandey, P., Kaushik, C., Dutt, A., Agarwal, A.: PySPH: a Python-based framework for smoothed particle hydrodynamics (2020)
73. Randles, P., Libersky, L.: Smoothed Particle Hydrodynamics: Some recent improvements and applications. Computer Methods in Applied Mechanics and Engineering **139**(1-4), 375–408 (1996)
74. Rankine, W.J.M.: On the stability of loose earth. Philosophical Transactions of the Royal Society London **147**(1), 9–27 (1857)
75. Reches, Z., Eidelman, A.: Drag along faults. Tectonophysics **247**(1-4), 145–156 (1995)
76. Rockfield: Eflen explicit manual. Rockfield Software, Swansea, UK, (version 4.10) edn. (2017)
77. Roscoe, K.H.: The influence of strains in soil mechanics. Géotechnique **20**(2), 129–170 (1970)
78. Rudnicki, J.W., Rice, J.R.: Conditions for the localization of deformation in pressure-sensitive dilatant materials. Journal of the Mechanics and Physics of Solids **23**(6), 371–394 (1975)
79. Saltzer, S.D., Pollard, D.D.: Distinct element modeling of structures formed in sedimentary overburden by extensional reactivation of basement normal faults. Tectonics **11**(1), 165–174 (1992)
80. Sanz, P.F., Borja, R.I., Pollard, D.D.: Mechanical aspects of thrust faulting driven by far-field compression and their implications for fold geometry. Acta Geotechnica **2**, 17–31 (2007)
81. Semnani, S.J., White, J.A., Borja, R.I.: Thermoplasticity and strain localization in transversely isotropic materials based on anisotropic critical state plasticity. International Journal for Numerical and Analytical Methods in Geomechanics **40**(18), 2423–2449 (2016)
82. Shaw, J.H., Shearer, P.M.: An elusive blind-thrust fault beneath metropolitan Los Angeles. Science **283**(5407), 1516–1518 (1999)
83. Song, X., Borja, R.I.: Finite deformation and fluid flow in unsaturated soils with random heterogeneity. Vadose Zone Journal **13**(5) (2014)
84. Song, X., Borja, R.I.: Mathematical framework for unsaturated flow in the finite deformation range. International Journal for Numerical Methods in Engineering **14**(9), 658–682 (2014)
85. Suppe, J.: Principles of Structural Geology. Prentice-Hall (1984)
86. Suppe, J., Medwedeff, D.A.: Geometry and kinematics of fault-propagation folding. Eclogae Geologicae Helvetiae **83**(3), 409–454 (1990)
87. Thebian, L., Najjar, S., Sadek, S., Mabsout, M.: Numerical investigation of dip-slip fault propagation effects on offshore seabed sediments. Engineering Geology **237**, 149–167 (2018)
88. Tran, H.T., Wang, Y., Nguyen, G.D., Kodikara, J., Sanchez, M., Bui, H.H.: Modelling 3D desiccation cracking in clayey soils using a size-dependent SPH computational approach. Computers and Geotechnics **116**, 103209 (2019)
89. Vardoulakis, I., Goldscheider, M., Gudehus, G.: Formation of shear bands in sand bodies as a bifurcation problem. International Journal for Numerical and Analytical Methods in Geomechanics **2**(2), 99–128 (1978)

90. Vignjevic, R., Djordjevic, N., Gemkow, S., De Vuyst, T., Campbell, J.: SPH as a non-local regularisation method: Solution for instabilities due to strain-softening. Computer Methods in Applied Mechanics and Engineering **277**, 281–304 (2014)
91. Violeau, D.: Fluid Mechanics and the SPH Method. Oxford University Press (2012)
92. Wang, G., Riaz, A., Balachandran, B.: Smooth particle hydrodynamics studies of wet granular column collapses. Acta Geotechnica **15**, 1205–1217 (2020)
93. Wang, H.N., Jiang, M.J., Zhao, T., Zeng, G.S.: Viscoelastic solutions for stresses and displacements around non-circular tunnels sequentially excavated at great depths. Acta Geotechnica **14**, 111–139 (2019)
94. Wang, Y., Bui, H.H., Nguyen, G.D., Ranjith, P.G.: A new SPH-based continuum framework with an embedded fracture process zone for modelling rock fracture. International Journal of Solids and Structures **159**, 40–57 (2019)
95. Wang, Y., Tran, H.T., Nguyen, G.D., Ranjith, P.G., Bui, H.H.: Simulation of mixed-mode fracture using SPH particles with an embedded fracture process zone. International Journal for Numerical and Analytical Methods in Geomechanics **44**(10), 1417–1445 (2020)
96. Wendland, H.: Piecewise polynomial, positive definite and compactly supported radial functions of minimal degree. Advances in Computational Mathematics **4**(1), 389–296 (1995)
97. Widuliński, Ł., Tejchman, J., Kozicki, J., Leśniewska, D.: Discrete simulations of shear zone patterning in sand in earth pressure problems of a retaining wall. International Journal of Solids and Structures **48**(7-8), 1191–1209 (2011)
98. Wolfe, F.D., Shaw, J.H., Plesch, A., Ponti, D.J., Dolan, J.F., Legg, M.R.: The Wilmington blind-thrust fault: An active concealed earthquake source beneath Los Angeles, California. Bulletin of the Seismological Society of America **109**(5), 1890–1906 (2019)
99. Xu, G., Gutierrez, M., He, C., Meng, W.: Discrete element modeling of transversely isotropic rocks with non-continuous planar fabrics under Brazilian test. Acta Geotechnica **15**, 2277–2304 (2020)
100. Xu, W.J., Liu, G.Y., Yang, H.: Study on the mechanical behavior of sands using 3D discrete element method with realistic particle models. Acta Geotechnica **15**, 2813–2828 (2020)
101. Zhan, L., Peng, C., Zhang, B., Wu, W.: A SPH framework for dynamic interaction between soil and rigid body system with hybrid contact method. International Journal for Numerical and Analytical Methods in Geomechanics **44**(10), 1446–1471 (2020)
102. Zhao, S., Bui, H.H., Lemiale, V., Nguyen, G.D., Darve, F.: A generic approach to modelling flexible confined boundary conditions in SPH and its application. International Journal for Numerical and Analytical Methods in Geomechanics **43**(5), 1005–1031 (2019)
103. Zhao, T., Liu, Y.: A novel random discrete element analysis of rock fragmentation. International Journal for Numerical and Analytical Methods in Geomechanics **44**(10), 1386–1395 (2020)
104. Zhao, Y., Borja, R.I.: A continuum framework for coupled solid deformation–fluid flow through anisotropic elastoplastic porous media. Computer Methods in Applied Mechanics and Engineering **369**, 113225 (2020)
105. Zhao, Y., Semnani, S.J., Yin, Q., Borja, R.I.: On the strength of transversely isotropic rocks. International Journal for Numerical and Analytical Methods in Geomechanics **42**(16), 1917–1934 (2018)